Atom-Level Tandem Catalysis in Lithium Metal Batteries

Jian Wang,* Jing Zhang, Yongzheng Zhang, Huihua Li, Peng Chen, Caiyin You, Meinan Liu, Hongzhen Lin,* and Stefano Passerini*

High-energy-density lithium metal batteries (LMBs) are limited by reaction or diffusion barriers with dissatisfactory electrochemical kinetics. Typical conversion-type lithium sulfur battery systems exemplify the kinetic challenges. Namely, before diffusing or reacting in the electrode surface/interior, the $Li(solvent)_x^+$ dissociation at the interface to produce isolated Li^+, is usually a prerequisite fundamental step either for successive Li^+ "reduction" or for Li^+ to participate in the sulfur conversions, contributing to the related electrochemical barriers. Thanks to the ideal atomic efficiency (100 at%), single atom catalysts (SACs) have gained attention for use in LMBs toward resolving the issues caused by the five types of barrier-restricted processes, including polysulfide/Li_2S conversions, $Li(solvent)_x^+$ desolvation, and Li^0 nucleation/diffusion. In this perspective, the tandem reactions including desolvation and reaction or plating and corresponding catalysis behaviors are introduced and analyzed from interface to electrode interior. Meanwhile, the principal mechanisms of highly efficient SACs in overcoming specific energy barriers to reinforce the catalytic electrochemistry are discussed. Lastly, the future development of high-efficiency atomic-level catalysts in batteries is presented.

1. Introduction

The increasing consumption of nonrenewable fossil fuels has given rise to climate change and environmental pollution.[1] To reach the world-wide objectives of "Carbon Peaking" and "Carbon Neutrality," developing high-energy-density lithium-ion batteries (LIBs) is requisite for portable electronic devices, vehicles, and large-scale smart grids.[2] LIBs are based on the mechanism of insertion/extraction of Li^+ between the positive electrode (cathode such as $LiNi_{0.8}Co_{0.1}Mn_{0.1}O_2$ (NCM) and $LiFePO_4$ (LFP)) and the negative electrode (anode such as graphite, silicon, and their mixtures as well as oxides) along with the migration of $Li(solvents)_x^+$ in the electrolyte, experiencing migration/diffusion barriers from interface to electrode interior.[3] However, state-of-the-art LIBs are far from achieving 500 W h kg^{-1} required to enable the 500 mile driving range owing to the capacity bottlenecks of cathode and anode.[4]

In comparison with conventional insertion-based cathode materials, such as LFP and NCM, which involve only one electron exchange per unit formula, conversion-type lithium metal batteries (LMBs), employing, e.g., sulfur or oxygen cathodes, store more than one electron per formula unit, enhancing the energy density and providing nearly 10 times higher energy density than that of LFP or NCM.[5] To elucidate the challenges of conversion-type LMBs, the representative lithium

J. Wang, H. Li, S. Passerini
Helmholtz Institute Ulm (HIU)
D89081 Ulm, Germany
E-mail: jian.wang@kit.edu; stefano.passerini@kit.edu

J. Wang, H. Li, S. Passerini
Karlsruhe Institute of Technology (KIT)
D76021 Karlsruhe, Germany

J. Wang, M. Liu, H. Lin
i-Lab and CAS Key Laboratory of Nanophotonic Materials and Devices
Suzhou Institute of Nano-tech and Nano-bionics
Chinese Academy of Sciences
Suzhou 215123, China
E-mail: hzlin2010@sinano.ac.cn

J. Zhang, C. You
School of Materials Science and Engineering
Xi'an University of Technology
Xi'an 710048, China

Y. Zhang
State Key Laboratory of Chemical Engineering
East China University of Science and Technology
Shanghai 200237, China

P. Chen
Jiangsu Key Laboratory of Materials and Technologies for Energy Storage
College of Materials Science and Technology
Nanjing University of Aeronautics and Astronautics
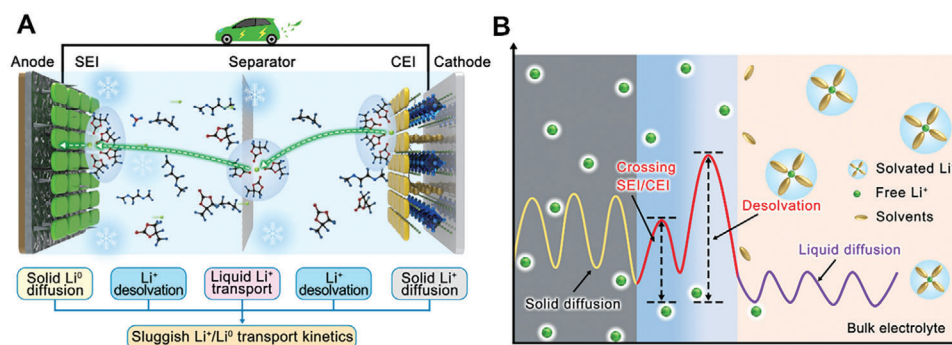Nanjing 210016, P. R. China

Figure 1. A) Charge/discharge evolution of lithium metal batteries (LMBs) with five typical electrochemical behaviors from electrolyte to electrode and B) corresponding energy barriers affecting the electrochemical kinetics.

sulfur batteries with high energy density of 2600 W h kg^{-1} are presented.[6] Moreover, elemental sulfur is very abundant, low-cost, and friendly to the environment. Specifically, sulfur undergoes stepwise interactions upon lithiation starting from S_8, going through soluble polysulfides ($Li_2S_8/Li_2S_6/Li_2S_4$) and eventually, insoluble products (Li_2S/Li_2S_2), displaying a net two-electron reaction. The metallic Li anode provides the relatively low potential and high capacity of 3860 mAh g^{-1}.[7] However, like LIBs, the conversion-type LMBs also encounter severe reaction/plating barriers from interface/surface to the electrode's interior owing to sluggish reaction kinetics in both the sulfur reduction reaction (SRR) and the sulfur oxidation reaction (SOR). The anode also goes along with the nonuniform Li$^+$ flux from the Li(solvents)$_x^+$ dissociation, inducing uncontrolled Li^0 deposition with dendrite growth.[8] In addition, parasitic reactions lead to electrolyte consumption in lithium-sulfur (Li−S) cells. The repeated charge/discharge activity would eventually deplete the electrolyte resulting in higher energy barriers causing low Coulombic efficiency (CE) and performance deterioration.[9]

To resolve these drawbacks, extensive efforts on the matrix designs or electrode surface modifications are made to the sulfur cathode and Li anode.[10] The battery performance is mostly determined by the kinetics of interfacial Li(solvents)$_x^+$ solvation/desolvation energies, and the subsequent Li$^+$ transport in the electrode bulk,[5c,11,12] affecting the overall reaction kinetics and barriers of polysulfide conversion, Li$_2$S delithiation, Li(solvent)$_x^+$ desolvation, Li$^+$ and Li^0 diffusion.[13] Catalysis strategies to decrease the electrochemical barriers have been proposed such as single atom catalysts (SACs).[14] In comparison with conventional catalysts, SACs showcase superiorities offering: 1) the highest activity in single site; 2) the maximum atom utilization (100%); 3) the largest surface area with 100% exposure; 4) tunable reactivity by regulating supports and/or chemical surrounding; and 5) negligible weight contribution to the system. Owing to these superior advantages, SACs are becoming very attractive for practical applications ranging from energy conversion systems to chemical synthesis. SACs can successfully accelerate the kinetics of polysulfide conversions in the sulfur/Li$_2$S electrode bulk and/or at the interface/surface.[13a] Recently, the successful applications of SACs in lithium anodes have shifted our insight to the atomic level interactions between Li$^+$/Li^0 and catalysts, transitioning from the static lithiophilic behavior into the dynamic evolution mechanism.[9b] The Li plating behavior is affected by the Li(solvent)$_x^+$ dissociation, Li$^+$ transport across the

solid electrolyte interphase (SEI), and Li^0 diffusion on the surface, which are responsible for the Li dendrite formation and elevated energy barriers.[12a,15] The reaction drives a cascade of interactions and plating, where Li$^+$ acts as the link and bridge for the reaction products at the cathode or anode side.[16] However, to date, the knowledge to realize uniform Li metal plating in LMBs from the aspect of kinetics modulations and the designs of ideal tandem catalyst has yet to be discovered.

In this perspective, we summarize the tandem reaction behaviors and the corresponding electrochemical barriers in conversion-type LMBs (**Figure 1A**). Typically, from electrolyte to the electrode interior, Li$^+$ experiences the status of Li(solvents)$_x^+$ in the bulk electrolyte, transfer across SEI/cathode electrolyte interphase (CEI) losing its solvation shell, and transport in the electrode interior, exhibiting multidimensional kinetic barriers (Figure 1B). Specifically, lithium sulfur battery systems are assessed to elucidate the barrier challenges. Initially, the energy barriers affecting the electrochemical kinetics of electrodes including sulfur conversions and Li plating are analyzed from the interface to the electrode bulk (Figure 1B). Owing to the ideal catalytic efficiency (100%) of SACs, both fast Li$^+$ exchange in liquid polysulfides or solid Li$_2$S and rapid interfacial Li(solvent)$_x^+$ desolvation, followed by free isolated Li$^+$ transfer across SEI, Li^0 nucleation and diffusion are driven, stimulating self-tandem catalysis capability (**Figure 2**). Despite progress in the electrochemistry of sulfur and Li electrodes, the principal mechanisms of SACs in overcoming these energy barriers to reinforce the catalytic electrochemistry are still at an initial stage. Therefore, based on the initially proposed self-tandem catalysis effect, the contributions of SACs in systematically addressing the five types of barriers including polysulfide conversion, Li$_2$S delithiation, interfacial desolvation, Li nucleation and Li diffusion are discussed from electrode/electrolyte interface to electrode bulk. Lastly, future research directions of atom-level catalysis are outlined.

2. Electrochemical Barriers in Tandem Reactions of LMBs

2.1. Introduction to Tandem Reaction and Related Tandem Catalysis

Generally, tandem reactions include two or more reactions as those widely used in organic synthesis where one or more
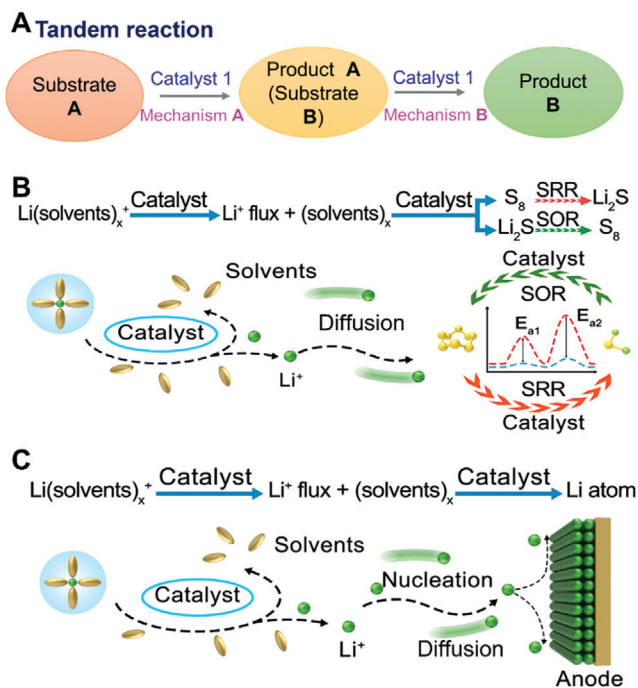
Figure 2. A) Tandem reaction and corresponding catalysis. Schematic illustration of the typical self-tandem catalytic reactions in B) the conversion-type sulfur cathode and C) the Li metal anode.

catalysts work for the chain of synthesis reactions.[17] When the same catalyst is used in the reaction, the reaction is also called "self-tandem" reaction. Typically, as illustrated in Figure 2A, two different reactions take place with the aid of catalysts while the latter reaction has the relationship with the former reaction, forming the tandem reactions. That is to say, the special material is not only the product (Product A) of the former reaction but also the reactant (Substrate B) in the latter reaction, serving as a reaction "bridge". Based on this, reaction kinetics in self-tandem reactions are related with the former reaction kinetics instead of the latter ones.[17b]

Taking the conversion-type Li-sulfur batteries as an example, the Li and S electrochemistry undergoes a series of tandem reaction process in a liquid electrolyte from the electrode/electrolyte interface to bulk interior.[5b,16,18] Meanwhile, the carrier in LMBs is the Li^+ with different state in the electrolyte or solid electrode's interior. Fast and uniform kinetics should be on the premise of more isolated Li^+ amount. Here, one can note that the desolvation process of the interfacial $Li(solvent)_x^+$ structure is initial and necessary for the successive reactions.[19] Specifically, in the cathode side, the tandem reactions include the interfacial $Li(solvent)_x^+$ dissociation and successive polysulfide conversion (Figure 2B). In the anode side, the Li metal anode experiences a stepwise Li plating/dissolution from Li^+ desolvation, electrochemical reduction of Li^+ to Li atoms, and finally migration of Li atoms to potential locations for nucleation (Figure 2C). In this section, the cascade behaviors in Li−S batteries and the corresponding formations of these five types of barriers are introduced in detail from interface to electrode interior.

2.2. Electrochemical Conversion Barriers in Conversion-Type Cathodes

2.2.1. Li^+ Desolvation/Diffusion Barrier at Sulfur/Electrolyte Interface

The first challenge for self-tandem reactions is the poor isolated Li^+ formation and diffusion kinetics across the interface, which affects the subsequent reaction kinetics (Figure 2B). Before arriving at sulfur/electrolyte interface, Li^+ tends to coordinate with solvent molecules to form $Li(solvents)_x^+$ complex. Thus, isolated Li^+ diffusion behaviors at the interface or interior cathode are closely related to the state of $Li(solvent)_x^+$ solvation structure.[12b,20] Owing to the effect of steric hindrance, the diffusion rate of partially dissociated $Li(solvent)_y^+$ ($y < x$) cluster complex across the interface is significantly lower in comparison with the bare isolated Li^+.[5c] Thus, it is necessary to dissociate the coordinated solvent molecules from the formed $Li(solvent)_x^+$ solvation sheath to form free isolated Li^+. Directly separating solvent molecules from the $Li(solvent)_x^+$ complex involves the breakage of related chemical coordination bonds, which can only be completed through overwhelming such high energy barriers.[20] The formed bare Li^+ can diffuse smoothly across the cathode/electrolyte interface and the interior cathode reacts with polysulfides rapidly only if the Li^+ desolvation process is kinetically accelerated.[21]

2.2.2. Polysulfide Conversion Barriers in SRRs

The sluggish electrochemical conversion kinetics of SRRs should be responsible for significant polysulfide shuttling and the subsequent degraded capacity.[22] In this regard, the sulfur molecular state experiences phase changes from solid to liquid and finally to solid again with the S−S bond breaking, corresponding to the typical four-step SRRs.[7] The polysulfide shuttling during transformation is closely related to their transformation time (t_T), defined as the limited time effect.[6b,7,23] When the migrating time of polysulfides from the matrix to the electrolyte (t_M) is shorter than that for their transformations ($t_M < t_T$), the shuttling effect occurs inevitably. In reverse, if the limited time effect is strengthened, i.e., $t_M > t_T$, the shuttle effect would be suppressed effectively. Meanwhile, the last transformation from Li_2S_2 to Li_2S ($Li_2S_2 + 2Li^+ + 2e \rightarrow 2Li_2S$ (solid → solid)) mainly dominates the reaction kinetics due to the sluggish electron/ion transfer in insulative Li_2S_2/Li_2S solids, which induces high energy barriers of the reduction kinetics and should be responsible for the large accumulation of polysulfide induced severe shuttling effect.[24] Therefore, it becomes a valid strategy to strengthen the limited time effect through declining the energy barriers in SRRs by utilization of highly active catalysts.

2.2.3. Li2S Decomposition Barrier in SORs

In the reversible charging process, the rate-determining step of the SORs is the Li^+ diffusion in the nonconductive Li_2S interior and interface. The initial delithiation evolution of Li_2S consists of the Li−S bond breaking with charge transfer and followed by

**ADVANCED
SCIENCE NEWS**

www.advancedsciencenews.com

**ADVANCED
MATERIALS**

www.advmat.de

Li^+ diffusion in the bulk solid Li_2S, both of which confront high energy barriers due to the insulative nature.[13a,25] Therefore, the SORs display sluggish transformation kinetics with high barrier, hindering the reversibility and giving rise to the irreversible utilization of sulfur.

Meanwhile, the classical Arrhenius formula can also depict this evolution:[26]

$$k = A exp^{-(Ea/RT)} \tag{1}$$

where k is reaction kinetics, A is the frequency factor, E_a is the activation barrier, R and T are the constants. Therefore, using the Arrhenius equation, lowering the activation barrier can improve the reaction kinetics in SORs, with the chance to achieve high sulfur utilization at high current rates.

2.3. Electrochemical Barriers in Metallic Li Plating

2.3.1. Desolvation Energy Barrier of Li(solvents)$_x^+$ Cluster

Generally, similar to cathode/electrolyte interface, isolated Li^+ does not exist in the electrolyte and usually coordinates with solvents, forming the Li(solvents)$_x^+$ solvation shell structure.[27] Before plating, the Li(solvents)$_x^+$ should be dissociated into isolated Li^+ and solvents at the interface (Figure 2C), respectively.[28] This means the sluggish step of releasing free Li^+ from the solvated clusters becomes the rate-limiting step for the successive interfacial Li^+ transfer and atom nucleation/diffusion.[29] The greater the coordination numbers in the Li(solvents)$_x^+$ cluster, the higher the desolvation energy barrier to overcome. Thus, reducing the desolvation barrier to achieve isolated Li^+ is one of the viable methods to weaken the bonding between Li^+ and solvent for facile desolvation.

2.3.2. Diffusion Barrier of Li$^+$ Across Interfacial SEI

After dissociating the Li(solvents)$_x^+$ clusters, the released Li^+ will transfer across the SEI layer, experiencing the two-phase surrounding changes from liquid to solid state. Upon contact, the generated isolated Li^+ should firstly penetrate through the solid SEI. Usually, the compact thinner SEI contributes to low transfer barriers owing to the short diffusion pathway.[13a] Thus, the physicochemical properties of the SEI affect interfacial Li^+ transport.[30] The metastable Li^+ is supposed to move to suitable sites for further nucleation through self-diffusion via vacancy and interstitial diffusion in the dynamic process. The hopping rate of an adatom on a periodic substrate can be expressed through the followed equation based on transition state theory:[31]

$$\nu = \frac{k_B T}{h} \exp\left(\frac{-\Delta F}{k_B T}\right) \tag{2}$$

where k_B and h are the Boltzmann constant and Planck's constant, ΔF is the Helmholtz free energy barrier for hopping between sites in the lattice, respectively. Although only the nearest-neighbor hopping model under the ideal condition is considered

in this equation with the lowest energy, the diffusion barriers of the Li^+ during the self-diffusion process should be overcome to drive rapid diffusion. Based on the self-diffusion, the high diffusion barriers and low surface activity of the SEI are the likely causes of this Li^+ sluggishness.

2.3.3. Diffusion and Nucleation Barriers of Li Atom on the Li Metal Surface

After Li^+ diffusion and/or hopping across SEI, the formation of initial Li atom coupled with electrons (with an applied constant current density) follows, where atom diffusion is nonsensitive to the electric field. The clusters of Li adatoms gathering to larger than critical size will grow to form crystal nuclei.[32] The dendrite formation can also be deemed as the larger aggregation of Li atoms with limited lateral diffusion. If a hemisphere is used to describe a Li nucleus formation on a substrate, the Gibbs formation free energy of this nucleus is defined by the surface energy change ($\Delta G_S = \gamma A$). And the interior bulk diffusion energy change is defined as $\Delta G_B = -N|\Delta \mu|$. Therefore, the free energy barrier affecting the spontaneous growth of Li atoms is determined by the competition between lowering the bulk free energy and increasing the surface energy as the equation below:[31]

$$\Delta G = \Delta G_B + \Delta G_S = -N |\Delta \mu| + \gamma A \tag{3}$$

where N is the number of Li atoms in the crystal cluster, $|\Delta \mu| = e\eta$ is the chemical potential difference for the single-electron electroreduction of Li, γ is the surface energy, and A is the surface area of the formed cluster. When the cluster grows to the critical nucleus with size of N^*, the free energy barrier for nucleation is expressed by the equation:[31]

$$\Delta G (N^*) = \frac{e\eta N^*}{2} \tag{4}$$

here the critical nucleus size (N^*) can be determined from

$$N^* = \frac{32\pi\gamma^3}{3\rho_s^2 (e\eta)^3} \tag{5}$$

where ρ_s is the number density of a bulk Li. For a semispherical Li nucleus, the critical radius is given by[31]

$$R = \frac{2\gamma}{\rho_s e\eta} \tag{6}$$

Based on Equations (4–6), we can find that $R \propto \gamma$ and $\Delta G(N^*) \propto R$ are revealed. It is the nucleation and the growth of the nucleus that will encounter elevated energy barrier. To eliminate the kinetic issues restricting Li anode, catalysts have been directed to lower the nucleation energy barriers and diminish the surface diffusion energy barriers to suppress ramified Li formation.[12a] In other words, dendrite-free plating can be readily implemented by lowering related lateral diffusion energy barriers and depositing on the target location of Li metal surface.

**ADVANCED
SCIENCE NEWS**

www.advancedsciencenews.com

**ADVANCED
MATERIALS**

www.advmat.de

As a proof-of-concept, five-related reaction steps of a lithium-sulfur battery are introduced in detail, for which SACs showcase great potential to decrease their energy barriers. Generally, catalysts are aimed to deal with the rate-determining steps. Owing to the different nature of energy barriers in tandem reactions, catalysts optimized to fit well one or two steps, probably, would not be very efficient to catalyze the other steps. For a specific step, such as desolation, the catalyst can be optimized for the best efficiency. The variety of transition metal SACs plays a universal role in interacting (complexing) with the reactant species, releasing the wanted product. Even if not optimized, SACs often decrease the diffusion/conversion barriers to some extent, i.e., even if SACs are optimized for one specific step, they can positively affect all other steps although at different extent. As a matter of fact, SACs have been proved to catalyze SOR process of Li_2S delithiation[13a,25a] and polysulfide conversions in the SRR process,[33] showing remarkable selectivity. On the other side, the effectiveness of SACs in accelerating the Li^+ desolation kinetics has been demonstrated resulting from the dramatic drop of the desolation energy barrier.[12b] With the optimization of chemical surrounding and catalytic site number, SACs are deemed to meet the needs of high-energy density lithium-sulfur batteries.

2.4. Electrocatalytic Methods to Assess Tandem Reaction Behaviors

Together with the above-mentioned theoretical simulations, the catalytic behavior can also be investigated experimentally. To this end, several electrochemical characterization methods to assess the catalytic behaviors on the kinetics of tandem reactions are:[5c,6b,19,34] 1) cyclic voltammetry (CV), providing the information on the catalytic effect on sulfur conversions, including, onset potential, redox overpotential, peak current and peak potential; 2) chronoamperometry, supplying information on the electrochemical conversions of polysulfides and Li_2S, including nucleation/dissolution; 3) potentiostatic intermittent titration technique (PITT), providing information on the time evolution of SRR and SOR process; 4) electrochemical impedance spectroscopy (EIS), supplying information on the Li ion and other charge transfer impedances, the Li ion diffusion coefficient, and, making use of the temperature dependence of the interfacial resistance, the activation energy of the desolation process; 5) rotating disk electrode (RDE), supplying information on the mass transport kinetics of sulfur species at the interface; 6) Tafel plot, visualizing the catalytic efficiency by supplying the overpotential, the slope, and the exchange current density.

3. SACs for Decreasing Interfacial and Interior Reaction Barriers

Although advances in inhibiting polysulfide shuttling effects have already been achieved by enhancing the adsorption ability (heteroatom-doped carbons, metal-based compound, modified polymers, etc.),[35] it is still not an effective method to realize high energy density with high utilization. Given this, the sluggish reaction kinetics of Li^+ transport at the interface or electrode interior should be responsible for the shuttling phenomena and

low sulfur utilization.[36] Currently, researchers have neglected the importance of the interfacial behaviors of $Li(solvents)_x^+$ cluster. As stated, with the highest ideal catalytic efficiency, SACs support the lowering of barriers for fast dynamic Li−S chemistry in SRR/SOR process.[8b,33,37]

3.1. Catalysts Decreasing $Li(solvents)_x^+$ Desolation/Diffusion Barrier at the Sulfur/Electrolyte Interface

Abundant free isolated Li^+ can achieve fast kinetics by reacting with sulfur.[6c,35a,38] In this regard, devising a stable yet highly catalytic layer at the sulfur/electrolyte interface to accelerate the dissociation of $Li(solvents)_x^+$ complex is of great importance to reach free Li^+. In any type of carbonate or ether-based electrolytes, additional energy is required to overcome the solvent dissociation from the solvation shell sheath, generating free Li^+ at the electrode/electrolyte interface.[12b] However, the studies of Li^+ desolation is still in its infancy for the cathode and few researchers are aware of the importance of desolation.[5c,19] Inspired by the self-tandem catalysis effect, our group had initially proposed a combined strategy of electrocatalysis and pore sieving to dissociate the $Li(solvents)_x^+$ structure to power the free Li^+ diffusion.[5c,19] Namely, a Li^+ diffusion booster is programmed to sieve large sized $Li(solvents)_x^+$ cluster to lower coordinated $Li(solvents)_y^+$ ($y < x$). As schematically illustrated in **Figure 3A**, the larger $Li(solvents)_x^+$ cluster is decomposed directly by the electrocatalytic sites, allowing the released smaller Li^+ or smaller $Li(solvents)_y^+$ species to penetrate through the pores.[19] At the same time, the outer solvation sheath layer can be sieved and adsorbed when these $Li(solvents)_y^+$ structures pass through the penetrating pores, which are observed by Raman spectroscopy with the enhancement ratio of contact ion pairs (CIP) and aggregates (AGGs) in the catalytic sieving systems. Meanwhile, the radial distribution function (RDF) also depicts the Li^+ shell coordination structures after catalytic sieving.[5b] Although there is a lack of SAC-related literature on cathodic desolation in Li−S batteries, according to the above described approach involving electrocatalytic porous nanoparticles in the cathode, it is reasonable to assume that SACs will also exhibit catalytic function in the desolation.

After desolation, the isolated free Li^+ should also transfer across the interface and the mobility of the isolated Li^+ is a decisive factor to the sulfur specie interaction.[6c] The sluggish Li^+ diffusion on the solid surface will hinder rapid conversion, thus displaying high overpotential gap.[39] For increasing catalytic efficiency and sites, our group had also reported on the influence of SACs on Li^+ diffusion in the Li_2S cathode or across the interface (Figure 3B–D).[13a] As displayed in Figure 3B, the Li ion diffusion barrier is confirmed to be highly sensitive to the dopant atoms. Especially, the metal atoms in nanocarbon that can guide and drive the transfer of the Li^+ across the interaction interfaces or along the carbon surface, so that a much lower energy barrier is achieved in the presence of SAC (0.089 versus 0.254 versus 0.256 eV) (Figure 3C).[13a] As a result, the Li_2S electrode with SACo does promote the Li^+ transport rate across the interface or on the matrix surface (Figure 3D). Consequently, the prepared high areal mass loading cells display high-rate performance at 5 C and a long cycle life of 200 cycles. These results demonstrate
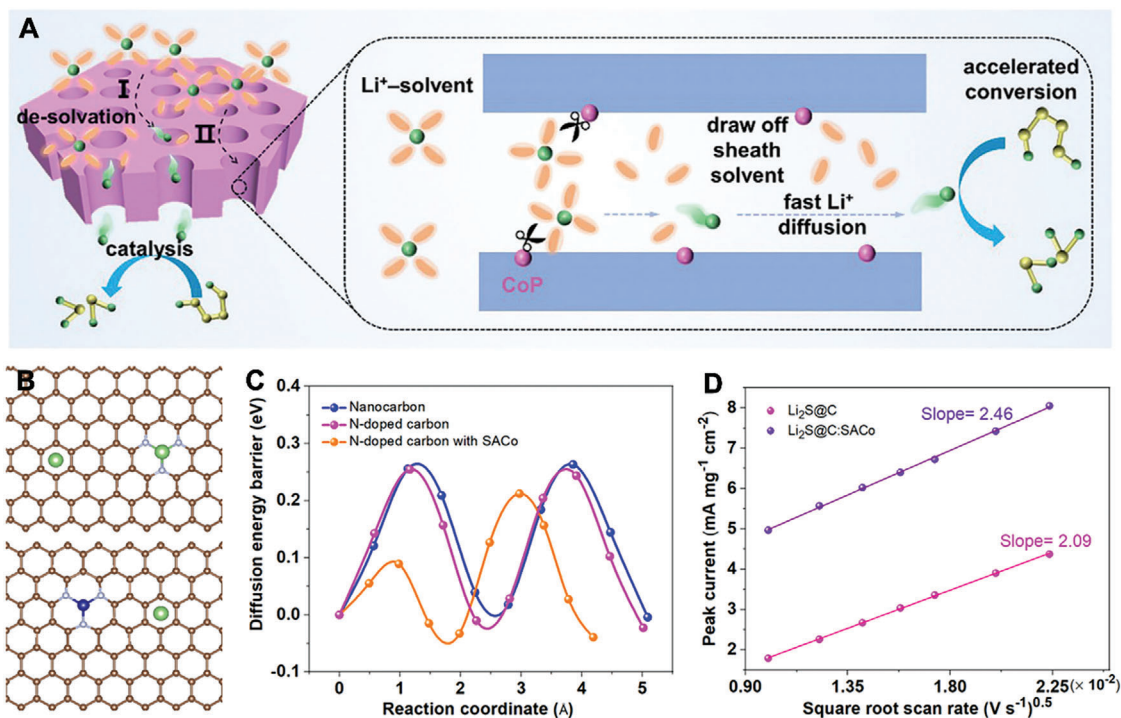
2402792 (5 of 18)

Figure 3. A) Schematic illustration of desolvation behaviors sieved by EPDB-CgCP. Reproduced with permission from[19] Copyright 2023, Wiley-VCH. B) Simulated lithium ion diffusion on the surface of nitrogen-doped carbon without/with single atomic Co (SACo). C) Comparison of lithium ion diffusion energy barrier on various nanocarbon. D) Plots of the peak currents versus the square root of the scan rates. Reproduced with permission from[13a] Copyright 2020, Elsevier.

the decreased Li$^+$ desolvation and diffusion barriers could significantly propel the reaction kinetics and thus increase the sulfur utilization.[5b,13a,19]

3.2. SACs in Decreasing the Reduction Barriers of SRRs

The electrochemical performance of a Li−S cell is strongly bound to the sulfur utilization. Thus, SACs may play a decisive role in the reducing kinetics barriers for the polysulfides-Li$_2$S conversion. To achieve high catalytic efficiency, the structure and/or the chemical properties of SACs need to be properly designed in terms of chemical coordination surroundings and electronic density modulation environment. The metal atoms of SACs have to be well dispersed on different matrices such as N-doped nanocarbons or defective compounds.[34] The catalytic efficiency lies in the catalytic site and size, chemical coordination surrounding, and electronic distribution environments.[40] For example, although SACs deliver ultrahigh catalytic activity, current SACs do not deliver optimal catalytic efficiency in SRRs owing to low atoms utilization from the size mismatch between the SACs and polysulfide molecules. Meng et al. uncovered the SAC aggregates existing as single Co cluster (between 5 and 14 Co atoms) with spatially resolved dimensions can commensurate the sulfur species and thus are fully accessible to enable 100% atomic utilization efficiency in electrocatalysis (**Figure** 4A).[40] Theoretical calculations further verify the more matchable pairs of the Li$_2$S$_6$ molecule with the two Co atoms (i.e., 0.40 and 0.32 nm, respectively) and more negative ΔG for the rate-limiting step (con-

version of Li$_2$S$_2$ to Li$_2$S). Over the charge/discharge process, the Co K-edge X-ray absorption near-edge structure (XANES) display the adsorption edge remained consistent with unchanged spectroscopic features, indicating the stability of the Co atom aggregates during the entire process (Figure 4B).

In the case of metal−nitrogen−carbon (M−N−C) configuration as active centers, the coordination numbers in the M−N configuration are supposed to affect the electronic distribution and catalytic site activities.[41] As revealed by Zhang et al., the electronic density structures of atomic Ni sites are regulated by changing the coordination number of N, facilitating in tuning their catalytic capabilities.[42] Accordingly, the simulated Ni-N$_5$/C structure shows the smallest kinetic barrier than the other M−N moieties, i.e., Ni−N$_3$/C and Ni−N$_4$/C models, and the barrier of the rate-limiting step is reduced by 0.62 eV (Figure 4C). To elaborate the catalytic conversion pathways, the in situ X-ray adsorption spectroscopy (XAS) is designed to monitor the S K-edge evolution during charge/discharge (Figure 4D).[33] Correspondingly, the peak evolutions of polysulfides and of Li$_2$S are recorded (Figure 4D,E), respectively. A clear rise in Li$_2$S corresponding to the early formation confirmed the improved electrochemical kinetics to form insoluble Li$_2$S$_2$/Li$_2$S under the Co atomic catalyst, indicating the concentration changes from polysulfides to Li$_2$S. Further, the critical role of the active-site geometry still needs to be revealed since the coordination-geometry tends to be changed when interacting with sulfur species. Through projected density of states (PDOS) of metal atoms below the Fermi level, the variation trends of electron occupation at different states are described (Figure 4F–I).[43] The partial occupied states of Co *3d*-orbitals
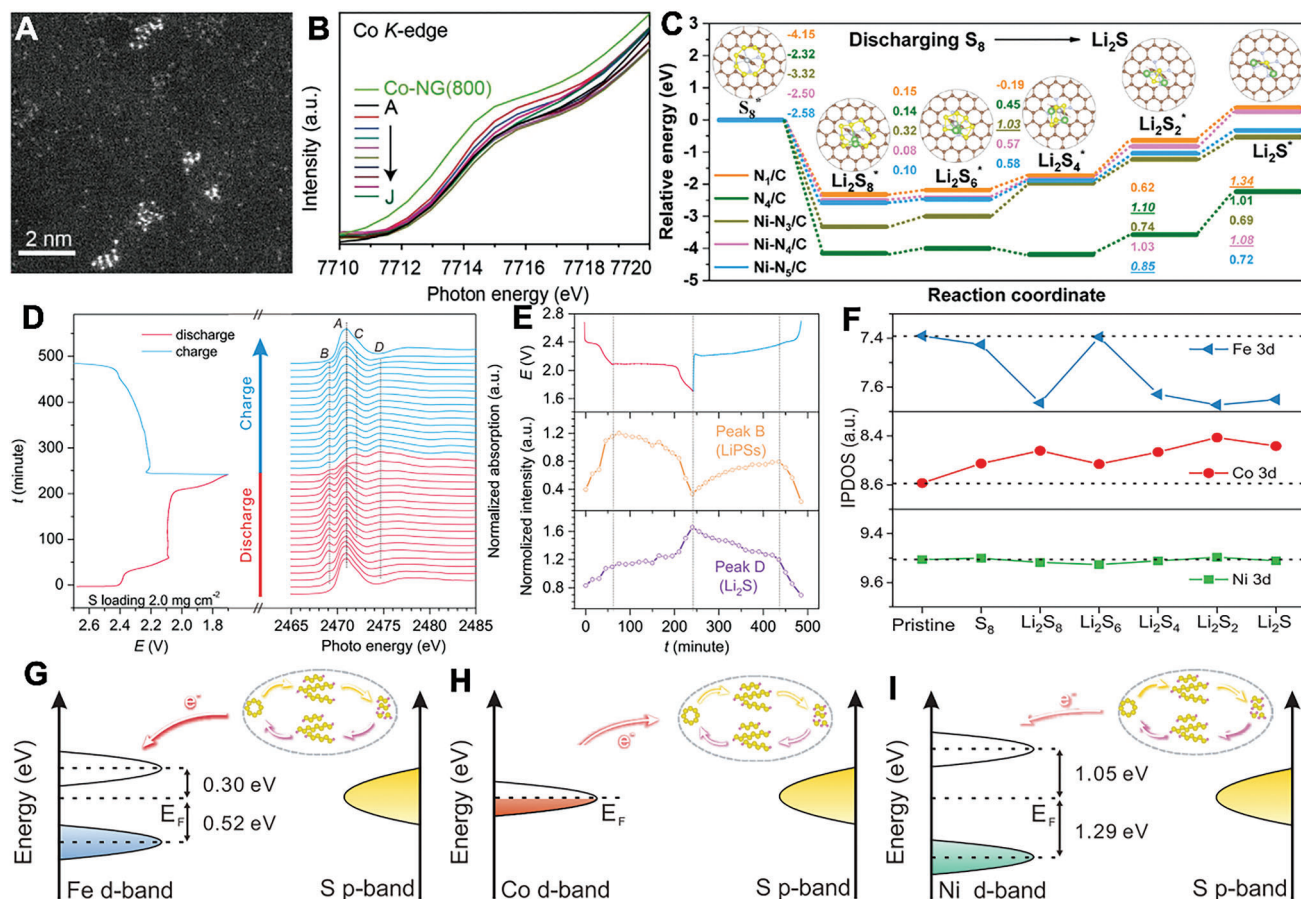
Figure 4. A) High-angle annular dark-field spherical aberration-corrected transmission electron microscopy (HAADF–STEM) images of the Co-NG recorded with different magnifications. B) Magnified profiles of the pre-edge region of Co K-edge X-ray absorption near-edge structure (XANES) spectra collected on the S@Co-NG cathode at different electrochemical states. Reproduced with permission from[40] Copyright 2021, The Authors. C) Energy profiles for the discharging process from S_8 to Li_2S on the five catalyst models that afford the optimized structures of LiPSs adsorption configurations. Reproduced with permission from[42] Copyright 2021, American Chemical Society. D) Evolution of S K-edge XANES during electrochemical cycling. E) Evolution of the intensities of peaks B and D representing concentration of polysulfides (LiPSs) and Li_2S respectively during electrochemical cycling. Reproduced with permission from[33] Copyright 2019, American Chemical Society. F) Schematic illustration of potential electron transformation through simulating the local electronic structure of Fe/Co/Ni 3d-orbitals near the Fermi level and the S p-orbitals structure of sulfur species. G–I) Variation trends of the calculated electronic occupation for Fe, Co, and Ni in interacting with different sulfur species, respectively. Reproduced with permission from[43] Copyright 2022, Wiley-VCH.

near the Fermi level make it prone to accept or lose electrons (Figure 4H). In short, the difference in hybridization between metal *3d*-orbitals and S *p*-orbitals of sulfur species promotes distinct electrochemical performance (Figure 4G–I).

3.3. SACs in Lowering the Delithiation/Diffusion Barrier of SORs

Besides catalyzing conversion kinetics to improve the available capacities, the ideal catalysts should also propel fast Li_2S decomposition since it is electronically/ionically insulative, contributing to huge delithiation barriers and dominating the SORs.[13a,25,44] The Li_2S delithiation includes the Li−S bond breaking with charge transfer and is followed by Li^+ transport for SOR taking place.[45] In 2018, our group had initially uncovered the catalytic roles of SAC in promoting the kinetics of cleaving the Li−S bond in Li_2S.[25a] Firstly, the decomposition barriers of pristine Li_2S with/without single atomic Fe (SAFe) were systemati-

cally compared with density functional theory (DFT) simulation. **Figure 5A** shows that the delithiation evolution activity is accomplished by extending the Li−S bond length to 2.29 angstrom, by which the highly active SAFe decreased the delithiation energy barriers from 3.4 to 0.81 eV (Figure 5B), a one forth decrease, facilitating the Li^+ transport in the Li_2S interior. To understand the catalytic delithiation mechanism of SACs, in situ XAS experiments along with detailed electrochemical analysis were performed (Figure 5C,D). The reduced and increased valence states of Fe K-edge are attributed to the interaction between SAFe and Li_2S/polysulfides due to the electronegativity and nucleophilicity of the sulfur atom (Figure 5D). Based on the theoretical and experimental investigation, a mechanism for the catalytic SAFe to speed up the electrochemical kinetics (Figure 5E) is outlined as follows:
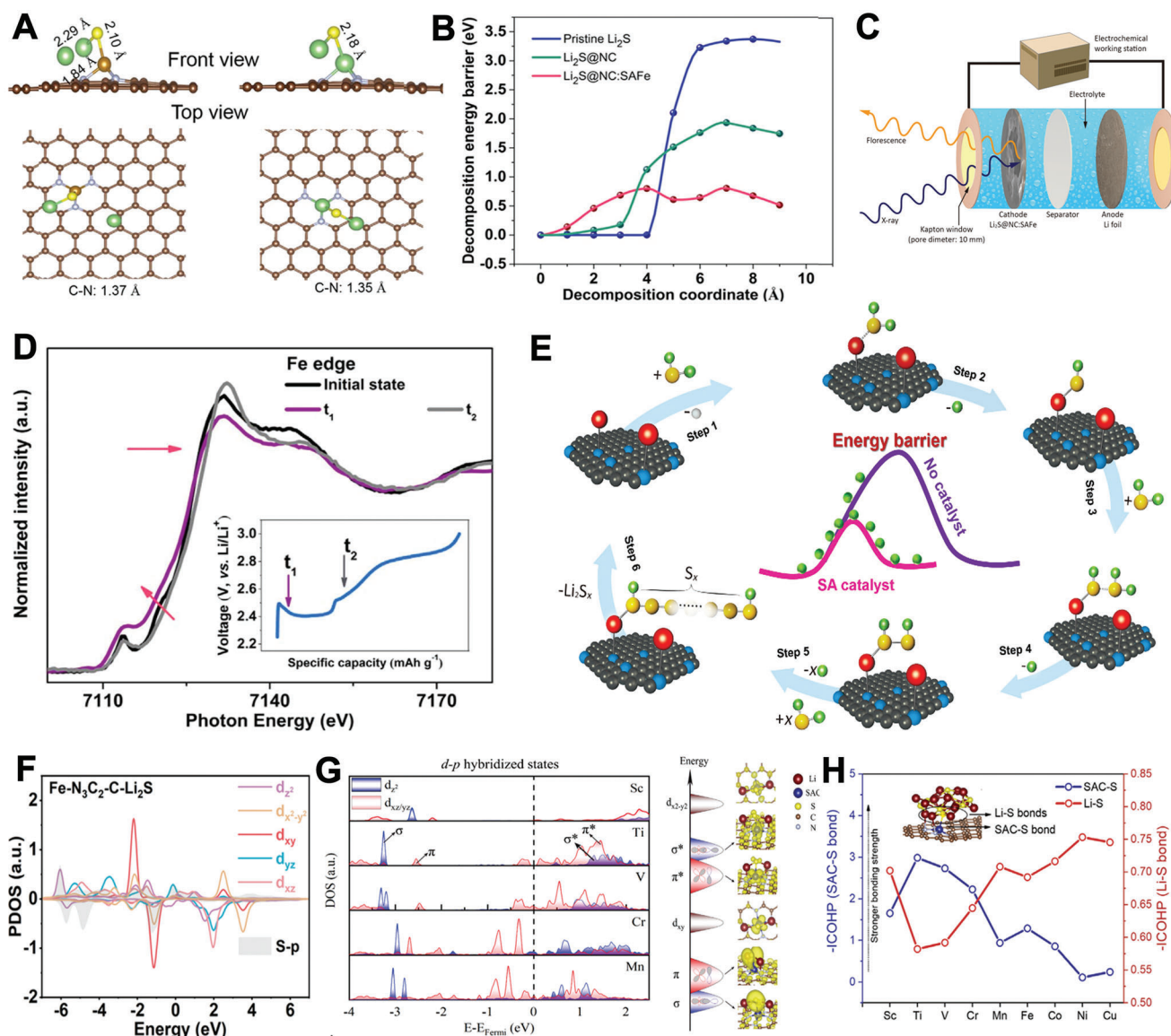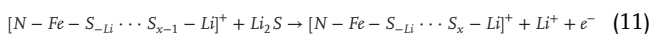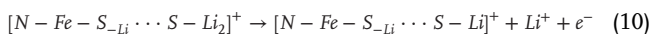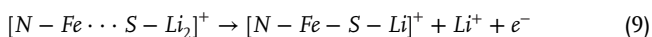
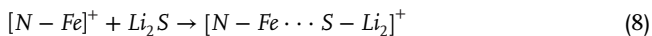$$[N - Fe] \rightarrow [N - Fe]^+ + e^- \tag{7}$$
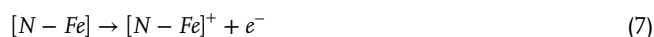
Figure 5. A) Calculated delithiation models of Li_2S with/without NC supported single atomic Fe (SAFe) catalyst. B) Simulation in delithiation energy barriers of the $Li_2S@NC$ with/without the SAFe catalyst. C) Designed configuration used for the in situ X-ray adsorption spectroscopy (XAS) measurements. D) In situ X-ray absorption near-edge structure (XANES) spectra obtained on the $Li_2S@NC$:SAFe cathode at 0.1 C under different charging states. E) Attempt on the putative mechanism for SAFe catalyzed Li_2S delithiation reaction. Reproduced with permission from[25a] Copyright 2018, Elsevier. F) Projected density of states (PDOS) of Fe and S in $Fe-N_3C_2-C-Li_2S$ and $Fe-N_4-C-Li_2S$ after interacting with Li_2S. G) d-p orbital hybridization design between single atom catalysts (SACs) and Li_2S. H) Strength of SACs-S and Li–S bonds evaluated by the integrated-COHP (−ICOHP) for the $(Li_2S)_8$-SACs adsorption system. Reproduced with permission from[48] Copyright 2021, Wiley-VCH.

$$[N-Fe]^+ + Li_2S \rightarrow [N-Fe\cdots S-Li_2]^+ \quad (8)$$

$$[N-Fe\cdots S-Li_2]^+ \rightarrow [N-Fe-S-Li]^+ + Li^+ + e^- \quad (9)$$

$$[N-Fe-S_{-Li}\cdots S-Li_2]^+ \rightarrow [N-Fe-S_{-Li}\cdots S-Li]^+ + Li^+ + e^- \quad (10)$$

$$[N-Fe-S_{-Li}\cdots S_{x-1}-Li]^+ + Li_2S \rightarrow [N-Fe-S_{-Li}\cdots S_x-Li]^+ + Li^+ + e^- \quad (11)$$

$$[N-Fe-S_{-Li}\cdots S_x-Li]^+ \rightarrow [N-Fe]^+ + Li_2S_x \quad (12)$$

when SAFe coordinates with Li_2S, the bond length of Li−S will be extended and weakened (Steps 1–2). Through this interaction, Li^+ could easily be decoupled from the intermediate $[N-Fe\cdots S-Li_2]$ with concomitant withdrawal of electron upon charging (Step 3). Similarly, the partially delithiated intermediate will continue to couple with another neighboring Li_2S molecule and finally generate a polysulfide chain via a repeated delithiation (Steps 4–5). The catalytic delithiation reaction will continue until the polysulfide chain is dissociated from SAFe at a certain charging state (Step 6). Thus, more Li_2S is exposed to the SAFe active site for a sustainable delithiation. Consequently, this SAC not only helps

ADVANCED
SCIENCE NEWS

www.advancedsciencenews.com

ADVANCED
MATERIALS

www.advmat.de

the initial delithiation by lowering the activation energy barrier but also boosts the cell's rate performance over an ultralong cycle life (588 mA h g^{-1} at 12 C and capacity fading rate of 0.06% per cycle for 1000 cycles at 5 C).

Apart from accelerating the breakage of the Li−S bond and Li$^+$ diffusion barriers, the poor electron exchange density between matrix and sulfur-related species may also impede the reaction kinetics, which is an indispensable factor for Li$_2$S delithiation.[46] However, the intrinsic electronic structure that determines the binding and kinetic energy barriers to reactions is still not clear.[47] Thereby, the electronic hybridization between d-orbitals of SACs and p-orbitals of sulfur is investigated. Liu et al. designed a precise electron engineering method to strengthen the d-p orbital hybridization.[48] The carbon-based SACs with Fe-N$_3$C$_2$ moieties (denoted as Fe-N$_3$C$_2$-C) showcase the p orbitals of S atoms in Li$_2$S and the d_{z^2} and d_{x^2/y^2} orbitals of Fe atoms in both Fe-N$_3$C$_2$-C and Fe-N$_4$-C moieties were overlapped, leading to the formation of σ- and π-bonds, respectively. However, the additional hybridization of d_{x^2/y^2} and d_{xy} orbitals in Fe-N$_3$C$_2$-C propels the formation of extra π-bonds with the p orbitals of S atoms (Figure 5F), delocalizing the electronic density distribution. In addition, Cheng's group proposed using transition metals with fewer filled anti-bonding states to construct a d-p hybridization to activate the interactions between atomic metal and sulfur (M−S) bond. In contrast to SAM (M = Sc, V, Cr, and Mn), SATi with only a few filled π* state becomes the most effective d-p hybridization while the M−S bond strength is relatively weak due to the large atomic radius of Sc (Figure 5G,H). In the SORs, the d-p hybridization strength and surrounding Li−S bonds are also evaluated by the integrated crystal occupation Hamiltonian population (ICOHP) value. As expected, the M−S bond strength gradually decreases from Ti to Cu (Figure 5H), accompanied by weakened surrounding Li−S bonds. Benefiting from this, SATi and SAV decrease the energy barriers significantly (≈50%) compared to the pristine carbon (≈2.1 eV).

Eight metal materials composed of atomic Fe, Mn, Ru, Zn, Co, Cu, V, and Ag on nitrogen-doped graphene (NG) were compared by Cui's group.[49] The single atomic substrate (Fe, Mn, Ru, Zn, Co, and V) materials maintain the structure stability during repeated charge–discharge cycles while the SACu@NG and SAAg@NG are unstable, which might be ascribed to the formation of metal sulfides. In virtue of the calculated screening, the SAV@NG composite displays the lowest decomposition barrier (1.10 eV) among all screened substrates, exhibiting both a maximum bond length (2.28 Å, Li−S) and a maximum bond angle (145.83°, Li−S−Li). As confirmed by experiments, both sulfur reduction and reverse Li$_2$S oxidation are significantly improved by the SAV@NG, achieving fast kinetics at 3 C with a reversible capacity of 645 mA h g^{-1}.

4. SACs for Dendrite-Free Plating with Lateral Li Diffusion

Metallic lithium has been regarded as the "holy grail" for the next-generation high-energy-density battery.[12a] However, metallic Li anode still suffers from several challenges including uncontrollable dendrite growth and unstable SEI, resulting in safety risks and low CE.[12a] In general, the Li plating process experiences a cascade process, which contains Li(solvents)$_x^+$ desolva-

tion, bare isolated Li$^+$ diffusion, electrochemical reduction of Li$^+$ to Li atoms, and finally migration of Li atoms to suitable locations for nucleation.[12a,38c] During these dynamic evolution steps, the plating process involves the formation and breaking of different types of chemical bonds, contributing to huge energy barriers.[9c] Kinetically modulating these barriers to achieve smooth deposition is the best strategy to achieve long cycle life. In this section, the emerging SACs for realizing dendrite-free lithium plating are introduced from decreasing energy barriers of Li$^+$ desolvation, Li^0 nucleation, and Li^0 diffusion.

4.1. Rapid Interfacial Li(solvents)$_x^+$ Desolvation Kinetics Accelerated by SACs

Before diffusion and nucleation, the generation process of free isolated Li$^+$ at the interface is always neglected by researchers. The dissociation of Li(solvents)$_x^+$ is a fundamental step in the uniformity of Li$^+$ flux and successive plating morphology.[50] The Li$^+$ desolvation kinetics may be regulated by electrolyte engineering. For example, appropriate solvents may reduce the strong Li$^+$-solvent binding, thus enabling desolvated Li$^+$ at the interface. However, this occurs at the expense of ion conductivity and/or current collectors' corrosion. Differing from electrolyte engineering, electrochemical catalysis enables propelling the interfacial dissociation kinetics of the Li(solvents)$_x^+$ shell structure, leading to free Li ions.[12b,26b] The Schottky defects in CeO$_2$ (CO) within carbon networks (SDMECO@HINC) were designed with delocalized electrons, creating numerous catalytic sites.[26b] Through interacting with the SDMECO@HINC catalyst, the faster desolvation kinetics of Li(solvents)$_x^+$ to form bare Li ions and lower nucleation overpotential is achieved and was briefly observed by interface-sensitive sum frequency generation (SFG) spectroscopy.

To probe the mechanism in catalyzing Li(solvents)$_x^+$ clusters, based on the electron-modulated defect sites in compounds, our group proposed an interfacial catalyst layer composed of "SAC-in-Defects" (SAFe/CVRCS@3DPC) on metallic Li for catalytically boosting Li$^+$ desolvation and Li^0 atom diffusion kinetics.[12b] Both Li(DOL)$_x^+$ and Li(DME)$_x^+$ solvation behaviors exist at the Li/electrolyte interface. As exhibited in **Figure 6A**, a higher desolvation barrier needs to be overcome in line with increasing coordination number (x) in the solvation shell. For example, Li(DME)$_4^+$ requires a dissociation energy of ≈37 kJ mol^{-1} to drive its decomposition into Li(DME)$_3^+$ and free DME molecule (Figure 6B). Once in contact with SAFe/CVRCS catalyst, the Li(DME)$_4^+$ desolvation behaviors proceed spontaneously (ΔG < 0) to decrease the solvation shell structure without costing additional energy. As indicated, the charge density in the Li(DME)$_4^+$ or Li(DOL)$_4^+$ complex tends to shift to SAFe/CVRCS surface, leading to the solvent's dissociation from Li$^+$ solvation sheath (Figure 6C). It is widely accepted that the desolvation behavior takes place at the electrode/electrolyte interface, however, there remains a lack of robust selective tools to monitor the asymmetric changes at the interface instead of the bulk electrolyte's interior.[50] Different from widely adopted Raman measurement, the Li$^+$ desolvation behaviors were selectively and initially probed by in situ SFG based on the spectroelectrochemical cell with/without bias voltage (Figure 6D,E).[12b] Accordingly, the
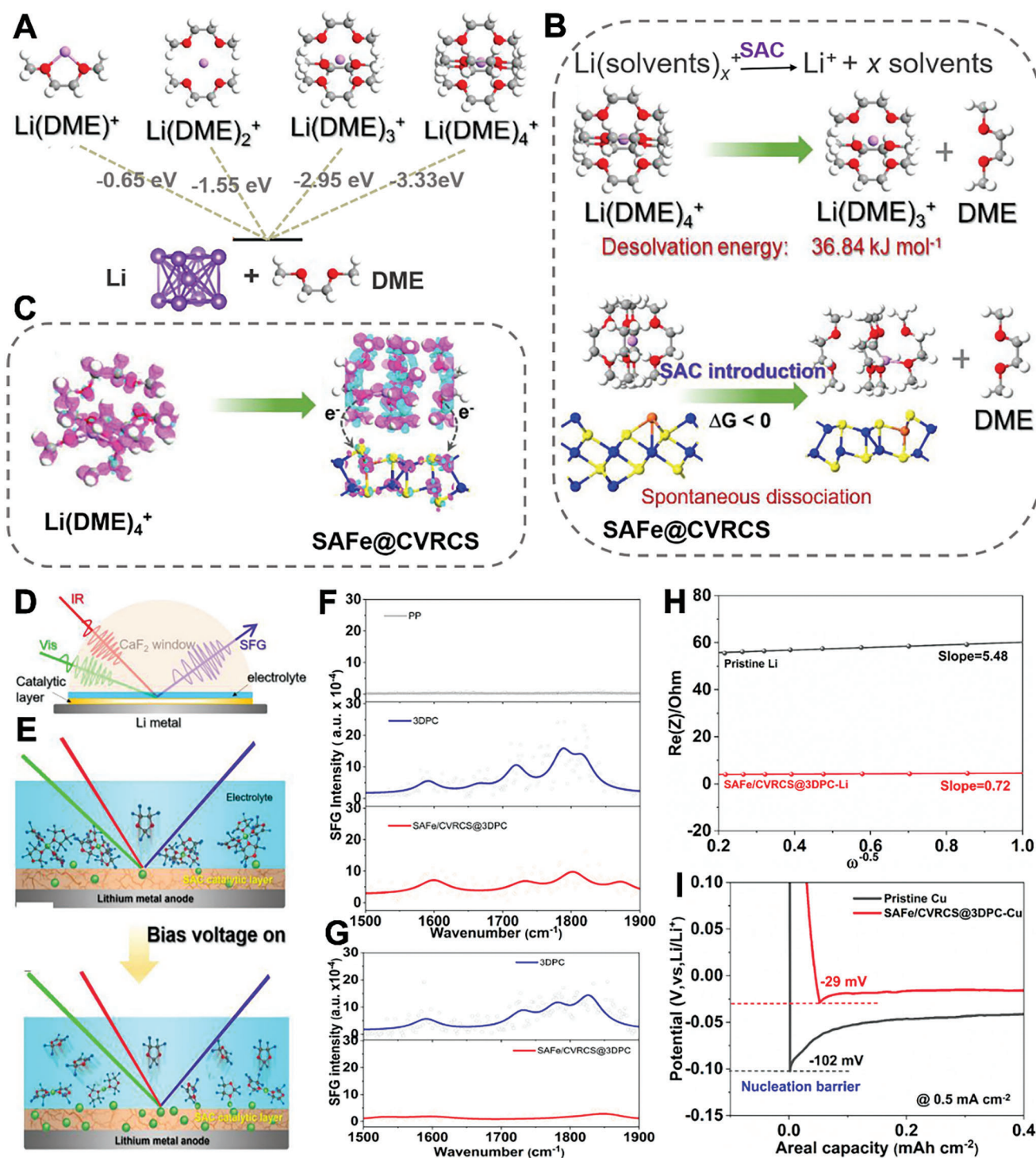
Figure 6. A) Reduction energy of Li solvation complex (Li(DME)$^{n+}$ calculated by density functional theory (DFT); desolvation barrier of Li(DME)$^{4+}$ into Li(DME)$^{3+}$ and DME in B) liquid electrolyte or on SAFe/CVRCS, respectively. C) Corresponding differential electron density transfer of Li(DME)$^{4+}$, SAFe/CVRCS substrate, and Li(DME)$^{4+}$ on SAFe/CVRCS, respectively. D) Schematic description of the in situ sum frequency generation (SFG) probing the electrolyte/catalyst interface. E) Molecular states of the Li$^+$ solvation structure in the electrode/electrolyte interface before and after turning the bias voltage on. F) SFG spectra of different adsorption states of Li$^+$ solvation structure under the C=O region and G) the corresponding decreased SFG intensities in the C=O region. H) Comparison of Li-ion transport with/without SAFe. I) Comparison of Li nucleation on SAFe/CVRCS@3DPC-modified Cu. Reproduced with permission from[12b] Copyright 2023, Wiley-VCH.

**ADVANCED
SCIENCE NEWS**

www.advancedsciencenews.com

**ADVANCED
MATERIALS**

www.advmat.de

signal intensities for solvent peaks of C=O bond and the typical C—H bond vibrations intensity were detected to be much lower on the SAC-decorated layer (Figure 6F,G). After applying a bias voltage of 20 mV onto these systems, the solvent peak position of the C=O and C—H vibrations remains unchanged, respectively. While both the SFG intensities are substantially reduced at the SAFe/CVRCS@3DPC//electrolyte interface, indicating the rapid dissociation of the Li(solvents)$_x^+$ complex catalyzed by SAFe/CVRCS@3DPC (Figure 6E,G), like the desolvation behaviors in the high concentration electrolyte as investigated by Raman spectroscopy. Stimulated by SAFe/CVRCS@3DPC catalytic layer, the Li ion diffusion kinetics was improved by ≈58 times with respect to the pristine one (Figure 6H), and the Li electrode displays a decreased nucleation barrier from 102 to 29 mV (Figure 6I). Consequently, the SAC modified Li-metal anodes stabilize smooth plating lifespan up to 1600 h and high CE without any dendrite formation.

Although the role of SACs in the Li$^+$ desolvation has been extensively discussed in the text related to Figure 6, their effects on the Li$^+$ desolvation and diffusion behavior under low temperature need to be investigated in the future. As the operative temperature decreases, the Li$^+$ solvation sheath may change, leading to more difficult interfacial desolvation, diffusion, and subsequently uncontrollable dendrite growth or "dead lithium" formation, i.e., deteriorating the cells' performance.[51] Usually, the electrolyte measures to enable low-temperature battery operation increase the solvation shell's volume by the participation of co-solvents or additives molecules, which increase Li$^+$-solvent bond length.[52] Affected by the even more sluggish diffusion kinetics at low temperature, the desolvation to generate free Li$^+$ at the interface is further impeded, resulting in nonuniform plating and dendrite growth. However, SACs may reduce the Li$^+$-solvent interaction to release free Li$^+$ from the solvation shell. Meanwhile, SACs may also help accelerating the interfacial diffusion, uniformizing the Li$^+$ flux for dendrite-free Li plating.

4.2. SACs in Decreasing the Li$^+$ Diffusion and Nucleation Barriers

To average the isolated Li$^+$ flux and decrease the diffusion barriers, the lightweight protective metal-based ceramic or alloy layers are constructed on the metallic Li surface.[53] For example, two diffusion methods namely vacancy and interstitial diffusion across alloy-based SEI layers are discovered.[54] However, the insufficient and unevenness sites go against the homogeneous Li plating, and the heavy weight of alloy metal layer reduces the energy density of Li anode.[9c,55] Decreasing the alloy particles down to atomic level could realize the maximum atomic utilization for highest activity.[56] After desolvation, the plating morphology is closely connected with the spatial distribution and migration capability of Li$^+$.[12b] To accelerate this, we proposed "SAC-in-Defects" strategy to anchor a metal heteroatom (SACo/ADFS@HPSC), which is revealed by XAS, high-angle annular dark-field spherical aberration-corrected transmission electron microscopy (HAADF–STEM), and electronic energy loss spectroscopy (EELS) (**Figure 7**A).[9a] For example, the bright dots in the STEM image represent the presence of Co atom embedded on defect-containing FeS nanoparticles (Figure 7B). With the

decreased charge transfer resistance, the SACo/ADFS@HPSC-Li electrode discloses a prolonged plating/stripping lifetime for 1600 h without short circuit at 0.5 mA cm^{-2} (Figure 7C), while the pristine Li only survives for less than 500 h under the same condition. As indicated in the Li−Cu cell, the nucleation barriers for Li$^+$ are decreased from 125 to 32 mV, indicating improved Li$^+$ kinetics for Li nucleation on the Cu electrode (Figure 7D). Too many cracks and collapses with dendrites were observed on the cycled pristine Li surface, however, the SACo/ADFS@HPSC-Li electrode retained a smooth and flat surface (Figure 7E–G). As schematically illustrated in Figure 7H, in the initial nucleation, the large number of active catalytic sites in SACo/ADFS are beneficial for regulating Li$^+$ flux for homogeneous nucleation. As the plating proceeds, the well-distributed fresh Li$^+$ tends to deposit smoothly without growing any dendrite, thus prolonging the lifespan of the cell. Accordingly, the high-loading Li−S pouch cell (5.4 mg cm^{-2}) powers the series of light emitting diodes (LEDs) with S pattern and satisfies the energy demand of a smart car with many sensors. Also, the cell stabilized for 60 cycles with the areal capacity of ≈3.7 mA h cm^{-2}, corresponding to the energy density of 1165 Wh kg^{-1} (Figure 7I,J).

In addition, Gong's group studied nucleation and dendrite-free deposition behaviors on the single metal atom-decorated nitrogen-doped graphene (SAM-NG), constructing a coordination of M−N$_x$−C (M, N, and C denoted as metal, nitrogen, and carbon atoms, respectively). The increased Li adsorption energy around the metal atomic sites is explained by the higher lithiophilic capability.[57] To unravel the relations between lithiophilic sites and nucleation, Sun et al. further performed the in situ optical microscopy image evolution, and the uniform nucleation and further smooth plating without any lithium dendrites can be achieved on Fe single atom-nitrogen-carbon (FeSA-N-C), while random nucleation and mossy lithium dendrites rapidly grow on bare Cu within 1 min (**Figure 8**A), confirming the ability of atomic Fe in smoothening Li$^+$ diffusion and nucleation.[58] A significant delocalization for the electron density distribution is formed on the entire plane of the atomic Zn sites (ZnSAs), indicating improved electronic conductivity (Figure 8B).[10d] With the introduction of atomic Zn sites, the surface energy to bind Li atom is decreased by 1.29 eV, implying that the binding reaction can take place on ZnSAs (Figure 8C). In terms of the migrating simulation, the Li migrates on ZnSAs surface with the smallest energy barrier, which demonstrates that Li could migrate easily toward the nearby areas for uniform nucleation rather than gathering locally to generate nanosized clusters.

Although different metal atoms have been investigated, systematic comparisons of different metal atoms are still rare and unknown. Recently, Gong's group systematically studied the binding energy of Li atoms on six types of nonnoble metal atoms (Mn, Ni, Co, Zn, Cu, Zr) anchored on the nitrogen-doped graphene (denoted as SAM@NG) via theoretical simulation.[59] The binding energies of Li atoms adsorbed on these designed lithiophilic sites are compared and the SAZr@NG shows the largest binding energy (−3.24 eV) (Figure 8D), which is close to that of the NG (−3.28 eV). Although the higher lithiophilic energy would cause potential uniform nucleation, the SAZr@NG did not behave well from experimental evaluation, suggesting that the lithiophilic binding energy cannot be served as the only index for predicting Li plating morphology. The stronger binding pair
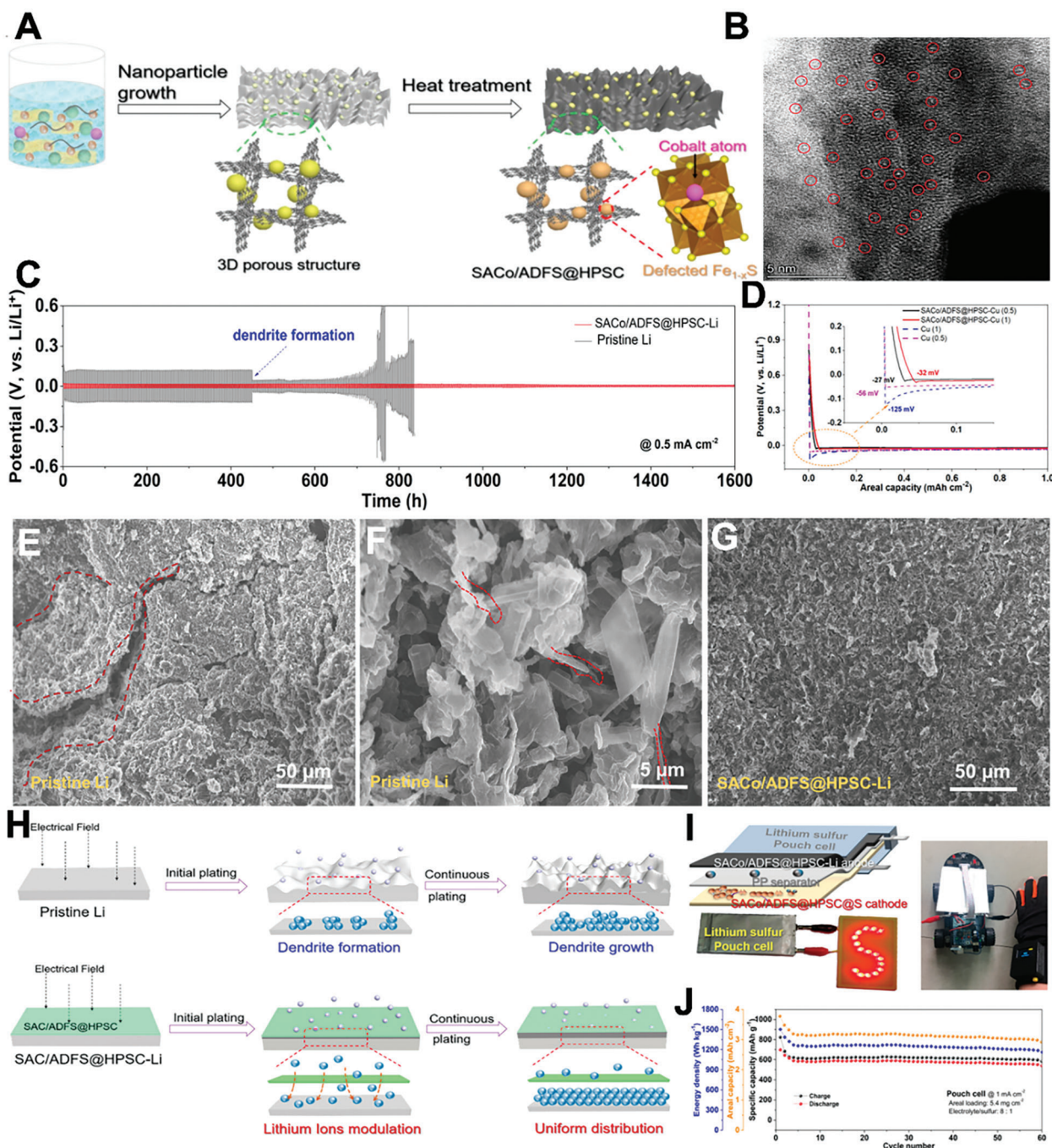
ADVANCED
SCIENCE NEWS

www.advancedsciencenews.com

ADVANCED
MATERIALS

www.advmat.de

Figure 7. A) Schematic description of the details in the synthesis of SACo/ADFS@HPSC. B) High-angle annular dark-field spherical aberration-corrected transmission electron microscopy (HAADF–STEM) image of SACo/ADFS@HPSC nanocomposites. C) Galvanostatic plating/stripping stability of the symmetric cells with SACo/ADFS@HPSC-Li and pristine Li electrodes. D) Comparison of voltage curves in asymmetric cells; SEM images of the E,F) cycled Li and G) SACo/ADFS@HPSC-Li. H) Schematic illustration of lithium plating on pristine Li and SACo/ADFS@HPSC modified Li electrode. I) Schematic configuration of large areal pouch cell, series of LED lights and smart cars with many sensors are powered by the as-prepared large areal pouch cell. J) Cycling performance of the large areal pouch cell. Reproduced with permission from[9a] Copyright 2021, American Chemical Society.

of SAZr@NG with Li atom causes obvious structural collapse on account of that Zr atom was pushed out of the plane significantly by the Li adsorption. In sharp contrast, the SAMn@NG structure with moderate binding energy improves the lithiophilicity effectively. On the other hand, the negligible change of bond length (0.005 Å) and bond angle (0.06°) of the SAMn@NG after Li interaction maintains the structural stability (Figure 8E). Overall, the lithiophilic sites with moderate Li adsorption energy are suitable to guide uniform deposition and keep the structure stable.
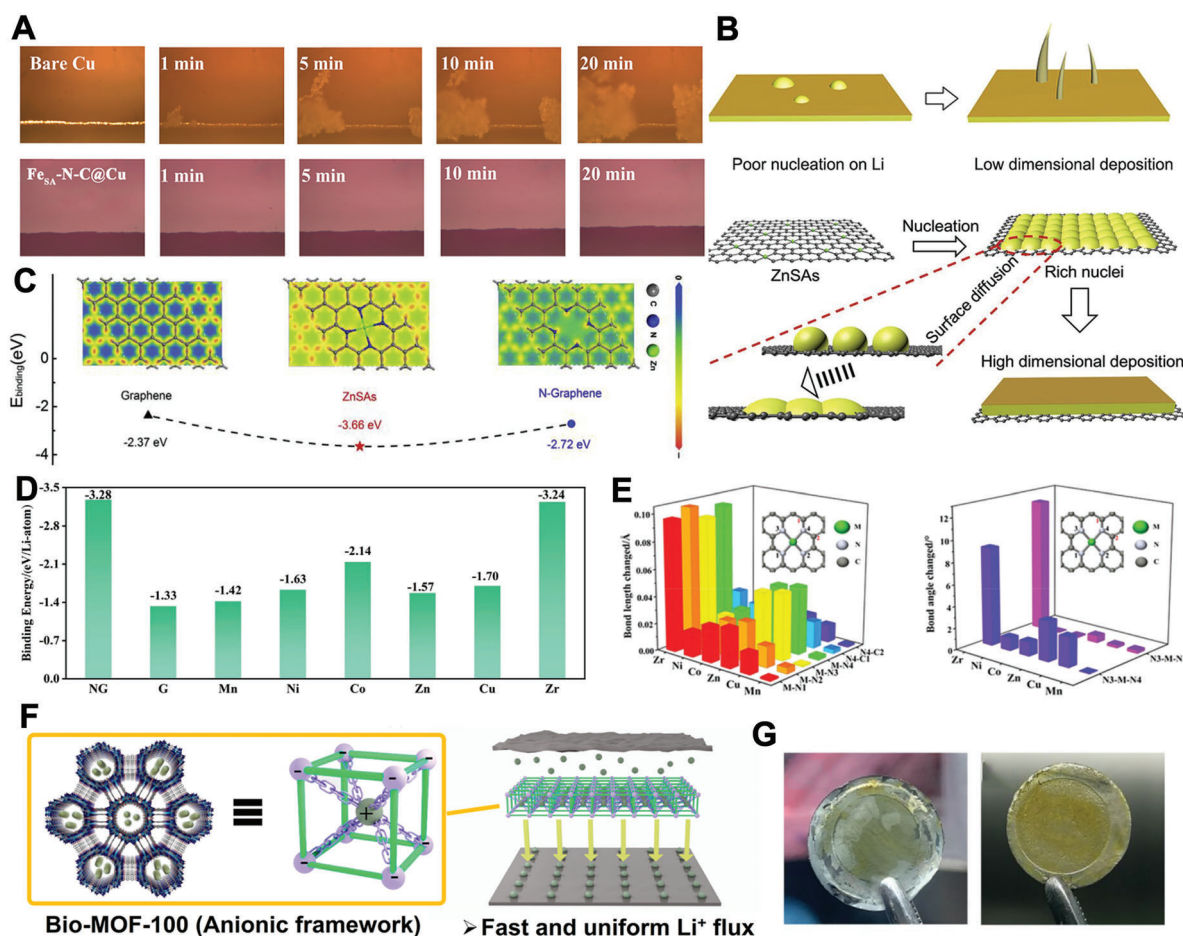
**ADVANCED
SCIENCE NEWS**

www.advancedsciencenews.com

**ADVANCED
MATERIALS**

www.advmat.de

Figure 8. A) Series of optical microcopy images of dendrite growth on bare Cu and FeSA-N-C@Cu; Reproduced with permission from[58] Copyright 2019, American Chemical Society. B) Electron density difference and surface binding energy of graphene, ZnSAs, and N-graphene. C) Schematic description of low dimensional deposition on bare Li and high dimensional deposition on single-atom Zn sites. Reproduced with permission from[10d] Copyright 2019, Elsevier. D) Binding energy comparison of Li atoms absorbed on different substrates. E) Relative calculations on bond lengths and bond angles between metal atoms and the surrounding N coordination before and after the deposition of Li atoms in the SAM@NG at different atomic positions. Reproduced with permission from[59] Copyright 2022, Wiley-VCH. F) Schematic illustration of SAZ-AF Janus separator with efficient inhibition of lithium dendrites upon fast Li ion diffusion. G) Photograph of the surface of the Bio-MOF-100/Celgard separator facing the Li anode and the corresponding Li anode of the cell after cycling. Reproduced with permission from[60] Copyright 2021, American Chemical Society.

After homogenization of the nucleus by the SAC strengthened lithiophilic sites, porous single-atom Zn-decorated embroidered ball-like nitrogen doped carbon derived from an anionic framework has the potential to sieve and modulate Li^+ behaviors for uniform deposition.[60] The anionic Bio-MOF-100 sieves the flux of Li^+ related species, enabling them to be quickly and uniformly transferred along the ordered channel (Figure 8F), achieving an outstanding cycling life of over 2800 h. As exhibited in Figure 8G, the Li metal anode with derived Bio-MOF-100 shows the ability of averaging the Li^+ flux distribution for smooth plating morphology and uniform nucleation.

4.3. Atom Diffusion Against Dendrite Aggregation Propelled by SACs

Two key problems for the growth of Li dendrites are the uneven distribution of Li^+ and the sluggish Li kinetics, restraining the lateral atom diffusion.[12a,19] To date, few groups focus on how the metastable Li atom behaves after coupling Li^+ with electrons. When the localized ability of fresh formed atom exceeds the diffusion ability, the whisker-shaped deposition appears to hasten the formation of fractal dendrite owing to the strong adsorption energy.[9b] To some extent, the aggregation of Li dendrite can be interpreted as the limitation of the lateral diffusion of metastable Li atoms with severe diffusion barrier.[12a,26b]

To achieve the dendrite-free Li plating under practical areal capacity, it is critical to boost Li atom diffusion along the lateral direction. In 2022, our group discussed the influence of Li atom diffusion on the plating behaviors.[9b] In the conventional lithiophilic theory, decreasing local current density via large surface-area conductive matrix presumes that Li^+ gain electrons from the matrix and deposit locally and separately. However, the reduced neutral Li^0 is not affected by the electric field, which is contradictory with the lithiophilic theory. DFT calculations display that a suitable adsorption energy is achieved ranging
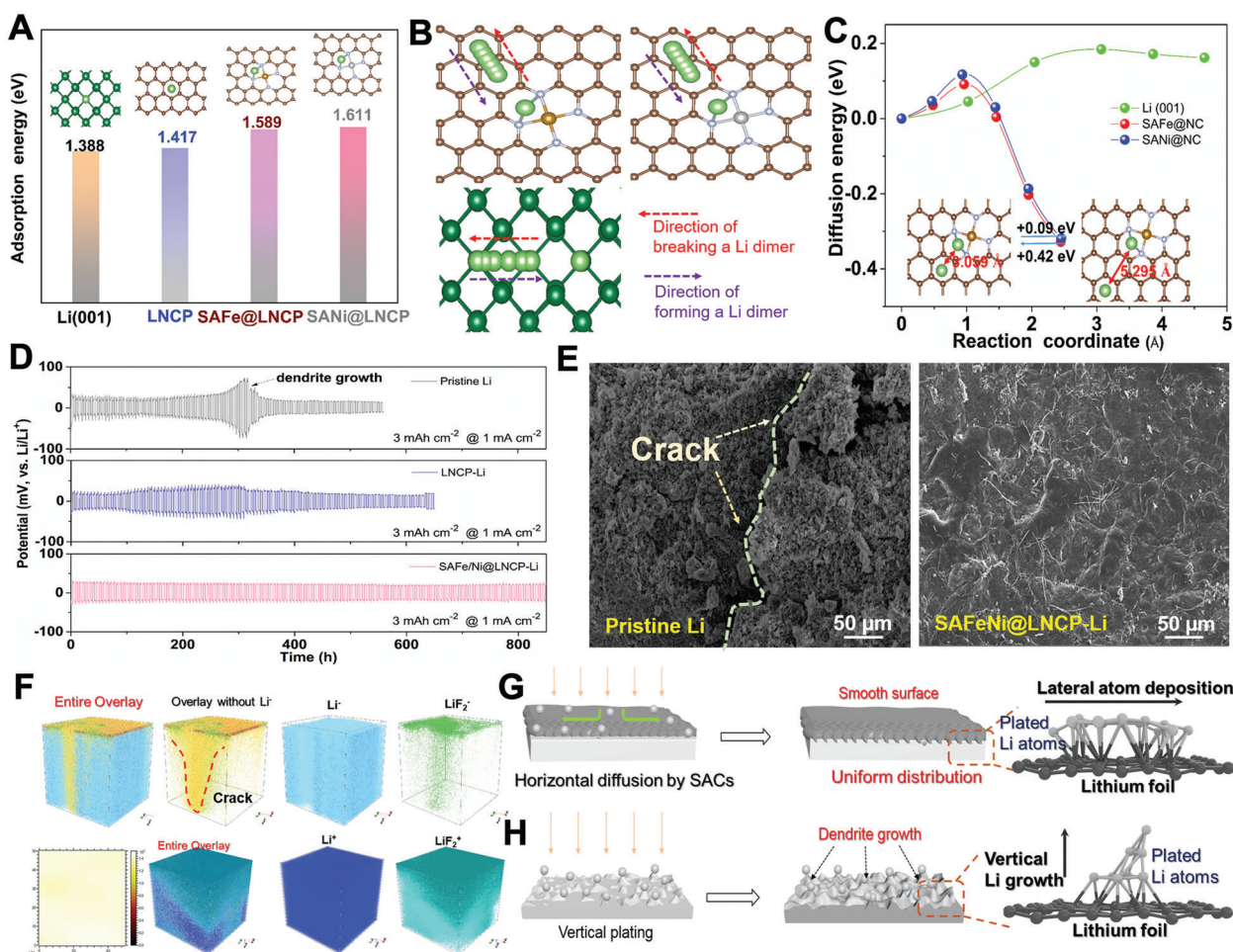
Figure 9. A) Li atom adsorption energy on various substrate surfaces. B) Top views of Li atoms in lithium dimer cleavage/formation process on simulated matrices and C) corresponding Li diffusion barriers. D) Galvanostatic charge/discharge comparison of the three electrodes. E) SEM images of the cycled Li electrode and the exposed Li surface after peeling off the upper SAFeNi@LNCP modulator. F) 3D morphology rebuild of the cycled pristine Li and SAFeNi@LNCP-Li by time-of-flight secondary ion mass spectrometry (TOF-SIMS). G,H) Possible plating/stripping mechanism on pristine Li and SAFeNi@LNCP-Li surface. Reproduced with permission from[9b] Copyright 2022, American Chemical Society.

from 1.589 to 1.611 eV by introducing SAC into the system (**Figure 9**A). To imitate the plating/stripping process, the diffusion energy barriers in forming or breaking a Li dimer are also investigated. As exhibited in Figure 9B,C, the lower breaking energies of 0.09 and 0.12 eV need to be overcome under the modulation of SACs in sharp contrast to 0.18 eV on the metallic Li (001) surface, demonstrating that the lithium atoms modulated by SACs preferentially diffuse in plane against local agglomeration and growth.

Supported by the theoretical simulations, a long stripping/plating lifespan of 850 h is achieved with ultrastable overpotentials for the optimized Li anode (SAFeNi@LNCP-Li) (Figures 9D) under 3 mA h cm^{-2}, which is superior to the state-of-the-art reports. The ex situ cycled SEM image displays smooth plated Li atoms under the motivation of SACs without any lithium dendrite formation, while the pristine Li electrode exhibits rough and loose structure with many cracks (Figure 9E). The time-of-flight secondary ion mass spectrometry (TOF-SIMS) further reconstructed the 3D species distribution of the cycled Li (Figure 9F). As diffusion accelerators, both the surface and over-

lay morphology display a smooth ionic distribution without any cracking such as LiF$_2^-$. With detailed characterizations, the fundamental diffusion mechanism is proposed (Figure 9G,H). Fast initial desolvation is propelled by the SACs and Li$^+$ flux is evenly distributed and averaged by the abundant SAC sites. When the plated Li atom (Li^0) forms at the SAC/Li interface, the surface diffusion rate along the lateral direction is significantly accelerated with the decreased barrier, allowing them to spread along planes uniformly over the electrode surface without vertical growth on any preferential site (Figure 9G). In strong contrast to the random vertical deposition with rugged surface and dendrite overgrowth on the pristine Li electrode (Figure 9H). Matching with high-capacity sulfur cathode, the Li−S full cell delivers high cycling and rate performance up to 5 C, showing great potential for the development of long-life and high-rate lithium batteries. As an overview, various single-atom catalysts increasing the electrochemical performance of the sulfur cathode and the Li anode in Li−S batteries are comprehensively compared in **Table 1** with respect to the synthesis method, metal atom, and related performance.

Table 1. Detailed comparison of single atom catalysts (SACs) in cathode or anode of Li–S batteries.

Electrode sample	Synthesis method	Metallic element	Overpotentials [mV]	Rate performance [mAh g^{-1}]	Initial performance [mAh g^{-1}]	Performance retention	Refs.
S@SA-Zn-MXene	Wet immersion method	Zn	140 @ 0.2C	517 @ 6 C	802 @ 1 C	88% after 400 cycles	[8b]
Li$_2$S@C:SACo	High-temperature pyrolysis	Co	260 @ 0.2 C	340 @ 5 C	982 @ 1 C	65.3% after 200 cycles	[13a]
Li$_2$S@NC:SAFe	Wet immersion method	Fe	350 @ 0.5 C	589 @ 12 C	1052 @ 1 C	60% after 1000 cycles	[25a]
S@Co-N/G	Impregnation-anneal	Co	160 @ 0.2 C	849 @ 2 C	930 @ 1 C	74.2% after 300 cycles	[43]
S@3DFeSA-CN	Pyrolysis	Fe	200 @ 0.2 C	783 @ 3 C	960 @ 1 C	38% after 2000 cycles	[46]
SATi@CF/S	Coprecipitation and anneal	Ti	200 @ 0.1 C	634 @ 3 C	920 @ 1 C	91.9% after 300 cycles	[48]
S-SAV@NG	Impregnation-anneal	V	230 @ 0.2 C	645 @ 3 C	780 @ 0.5 C	70.6% after 400 cycles	[49]
SAZ-AF Janus separator	Impregnation-anneal	Zn	650 @ 5 C	701.6 @ 5 C	1350 @ 1 C	67.8% after 200 cycles	[62]
SAFe@g-C$_3$N$_4$	High-temperature exfoliation	Fe	190 @ 0.1 C	704 @ 5 C	915 @ 2 C	90% after 200 cycles	[37]
S@Co–N/G	Refrigerate drying method	Co	200 @ 0.1 C	618 @ 4 C	1210 @ 0.2 C	84% after 500 cycles	[33]
SA-Fe/Fe$_2$N@NG	Polymerization and Pyrolysis	Fe	100 @ 0.1 C	904.8 @ 4 C	1128 @ 0.1C	84.1% after 500 cycles	[34]
Co-NG	Hydrothermal and annealing	Co	200 @ 0.1 C	648 @ 6 C	972 @ 0.5 C	52% after 600 cycles	[40]
Co–SAs@NC	Pyrolysis	Co	100 @ 1 C	670 @ 10 C	1069 @ 0.1 C	83% after 150 cycles	[41]
Ni-N5/HNPC/S	Wet impregnation	Ni	200 @ 0.2 C	684 @4 C	1188 @ 0.2C	81% after 500 cycles	[42]
SACo/ADFS@HPSC	Wet impregnation	Co	18 @ 0.5 mA cm^{-2}	140 mV @ 5 mA cm^{-2}	18 mV @ 0.5 mA cm^{-2}	18 mV after 1600 h	[9a]
SAFeNi@LNCP	Thermal Pyrolysis	Fe/Ni	50 @ 5 mA cm^{-2}	50 mV @ 5 mA cm^{-2}	25 mV @ 1 mA cm^{-2}	50 mV after 650 h	[9b]
ZnSAs	Atom-protected method	Zn	29 @ 1 mA cm^{-2}	240 mV @ 6 mA cm^{-2}	29 mV @ 1 mA cm^{-2}	29 mV after 800 h	[10d]
SAFe/CVRCS@3DPC-Li	Hydrothermal and treatment method	Fe	18 @ 0.5 mA cm^{-2}	73 mV @ 5 mA cm^{-2}	27 mV @ 0.5 mA cm^{-2}	18 mV after 1600 h	[12b]
SANi-NG	Impregnation-anneal	Ni	19 @ 0.5 mA cm-2	50 mV @ 4 mA cm^{-2}	19 mV @ 0.5 mA cm^{-2}	12 mV after 600 h	[57]
NGPE	Polymerization method	Co/Zn	15 @ 0.1 mA cm^{-2}	83 mV @2 mA cm^{-2}	176 @ 0.2 C	75% after 500 cycles	[63]
FeSA-N-C@Cu	Impregnation-anneal	Fe	25 @ 1 mA cm^{-2}	/	159 @ 1 C	89.3% after 200 cycles	[58]
SAMn@NG	Impregnation-anneal	Mn	56 @ 1 mA cm^{-2}	123 @ 2 C	144 @ 1 C	90% after 210 cycles	[59]

5. Summary and Future Perspectives

Lithium metal batteries based on conversion-type cathodes have attracted increased interests due to their favorable features such as offering higher energy density. However, the huge reaction barriers in desolvation and diffusion with dissatisfactory electrochemical kinetics prevent their further commercialization, where the interfacial Li$^+$ desolvation is the prerequisite for the successive reaction or plating. Taking a typical example of Li−S batteries, the tandem characteristics of battery reactions have been systematically analyzed. Specifically, catalysts in addressing barriers of desolvation and "reactions" are introduced from the electrode/electrolyte interface to bulk electrode interior. Future efforts and considerations toward achieving high-performance Li metal batteries with tandem catalysts are outlined in the following four sections (**Figure 10**):

5.1. Screening Sustainable Scalable Methodology for Enhancing Efficiency of Self-Tandem Reaction Kinetics

As a typical self-tandem reaction mold, the fast dissociation kinetics from Li(solvent)$_x^+$ complex to generate bare free Li$^+$ and fast ion diffusion kinetics across the interface should be the primary

2402792 (15 of 18)

**ADVANCED
SCIENCE NEWS**

www.advancedsciencenews.com

**ADVANCED
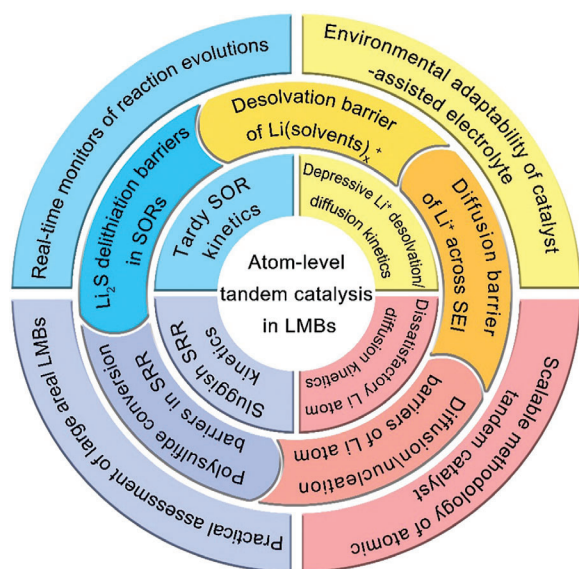MATERIALS**

www.advmat.de

Figure 10. Summary and perspective of atomic-level tandem catalysis in conversion-typed lithium metal batteries (LMBs).

premise for the Li electrodeposition and sulfur conversions. The interfacial Li$^+$ desolvation and reaction kinetics are closely related with catalytic sites and numbers. Although SACs with unique electronic state are associated with the redistribution of the electronic state between the catalyst and reactant, the loading concentration of single atoms heavily depends on the synthesis method. The specific area and doping content of N determine the concentration, uniformity, and stability at this stage, which is hard to scale up. Defective anchors employed with adjustable electronic density offer the potential to provide controllable coordination numbers to modulate the geometric structure. It could anchor and disperse high concentration metal atoms onto defective sites through strong metal-support interactions against aggregations. Future investigations may emerge from the overdiscussed M-Nx-C coordination structure and focus on the development of various kinds of defective support-SACs pairs with highly adjustable electron density to fasten the self-tandem reaction kinetics for sustainable Li metal batteries.

Thanks to the rapid development of artificial intelligence technology, machine learning will help to design SACs and/or new structures avoiding tedious and time-consuming experiments. Finite element methods and molecular dynamic simulations can well describe the effect of solvation evolution and atom diffusion on inhibiting dendrite formation. For instance, taking advantage of the simulation results regarding the decrease of Li$^+$ or Li^0 diffusion energy barriers, metal atom catalysts for the Li anode side can be selected for the further experiment validation. In summary, making the full use of machine learning is expected to accurately guide the material synthesis direction and significantly simplify the experimental steps.

5.2. Modulating Desolvation and Diffusion Kinetics in the Electrolyte for Low-Temperature Batteries

The electrochemical performance of LMBs in the carbonate/ether-based electrolytes is strongly dependent on

the surrounding temperature. Reducing the working temperature down to 0 °C, the viscosity for electrolytes becomes sticky and Li$^+$ solvation shell structure grows larger with higher stern effect, hindering the kinetics of the interfacial Li$^+$ desolvation and even Li$^+$ diffusion at the interface and interior. Current strategies mainly focus on the optimization of electrolyte engineering to regulate the solvation shell in the electrolyte interior. As discussed, the tandem reactions in batteries take place at the electrode/electrolyte interface. From previous studies, catalytic strategies allow to dissociate the Li(solvents)$_x^+$ rapidly to achieve more isolated Li$^+$ and propel the ion/atom diffusion. The SACs with highly adjustable electron density are potential candidates for the future low-temperature kinetic modulators. As research advances, the highly active SACs should act as interfacial promoter or suspended modulators in electrolytes, regulating the solvation structure and interfacial construction simultaneously to enhance the Li$^+$ transport kinetics on the interface under low temperature.

5.3. Real-Time Characterizations for Tracing Atom-Level Diffusion/Plating Evolution

Various in situ/operando characterizations have been proposed to track the real-time transformation of sulfur species, however, attention must be given to the visual evolution of the Li atoms diffusion. The current understanding of the self-tandem Li electrodeposition from the Li$^+$ desolvation to Li$^+$ diffusion and finally to the metastable Li atoms diffusion are largely constructed via computational simulations and macrolevel experiments. Unfortunately, the availability of in situ real-time observations to trace the dynamic states of the SACs are few, which is critical to comprehend the catalytic mechanism in dendrite-free Li electrodeposition. Hence, urgency resides in developing enhanced morphological, structural, and mechanical in situ/operando characterizations (such as in situ SEM, transmission electron microscopy (TEM), atomic force microscopy (AFM), Raman, and SFG for the inspection of the interfacial SEI evolution from the molecular/atomic level with the interaction of the metallic single atoms.[61] The low-temperature atom-level scanning tunnel microscopy (STM) can visualize the lithium atom diffusion on the metallic Li surface with the help of catalysts. Such real-time characterizations can provide synergy between computational modeling and experimental verification to elucidate the catalytic mechanisms in lateral and uniform Li plating.

5.4. Assessment of Scalable Large Li Metal Based Full Pouch Cells

The cycle life and the electrochemical performance of Li−S batteries depend on the inhibition of the polysulfide shuttle and Li dendrite formation. In fact, from a dynamic point of view, the capacity and energy density (and their stability upon cycling) of Li−S cells are determined by the utilization of sulfur and Li. During cell operation, the sluggish kinetics along with high barriers are responsible for the slow rates of polysulfide/Li$_2$S conversion, Li(solvent)$_x^+$ desolvation, and Li^0 nucleation/diffusion. SACs can reduce the conversion barriers inhibiting polysulfide

shuttling and Li dendrite formation, significantly extending the lifespan, and increasing the energy density along with the sulfur utilization. Ultimately, SACs may enable high areal capacities, which are necessary to achieve application for high-energy-density storage. However, dendrite-free Li plating behaviors and the related theoretical simulations (desolvation, nucleation, and diffusion barriers) should be conducted under harsh conditions, i.e., testing under high current density and low temperature, coupling with thinner Li foil and low electrolyte amount. Based on this premises, large pouch cells should be utilized to assess the above-mentioned strategies for practical applications.

Acknowledgements

Conflict of Interest

The authors declare no conflict of interest.

Keywords

[1] S. C. Kim, X. Gao, S.-L. Liao, H. Su, Y. Chen, W. Zhang, L. C. Greenburg, J.-A. Pan, X. Zheng, Y. Ye, M. S. Kim, P. Sayavong, A. Brest, J. Qin, Z. Bao, Y. Cui, *Nat. Commun.* **2024**, *15*, 1268.

[2] Y. Zhang, B. Johannessen, P. Zhang, J. Gong, J. Ran, S. Z. Qiao, *Adv. Mater.* **2023**, *35*, 2306923.

[3] Y. Jiao, F. Wang, Y. Ma, S. Luo, Y. Li, A. Hu, M. He, F. Li, D. Chen, W. Chen, T. Lei, Y. Hu, *Nano Res.* **2022**, *16*, 8082.

[4] Z. Liang, J. Shen, X. Xu, F. Li, J. Liu, B. Yuan, Y. Yu, M. Zhu, *Adv. Mater.* **2022**, *34*, 2200102.

[5] a) L. Zhou, D. L. Danilov, F. Qiao, J. Wang, H. Li, R. A. Eichel, P. H. L. Notten, *Adv. Energy Mater.* **2022**, *12*, 2202094; b) L. Li, H. Tu, J. Wang, M. Wang, W. Li, X. Li, F. Ye, Q. Guan, F. Zhu, Y. Zhang, Y. Hu, C. Yan, H. Lin, M. Liu, *Adv. Funct. Mater.* **2023**, *33*, 2212499; c) X. Li, Q. Guan, Z. Zhuang, Y. Zhang, Y. Lin, J. Wang, C. Shen, H. Lin, Y. Wang, L. Zhan, L. Ling, *ACS Nano* **2023**, *17*, 1653; d) J. Wang, S. Cheng, W. Li, S. Zhang, H. Li, Z. Zheng, F. Li, L. Shi, H. Lin, Y. Zhang, *J. Power Sources* **2016**, *321*, 193.

[6] a) Y. Song, L. Zou, C. Wei, Y. Zhou, Y. Hu, *Carbon Energy* **2022**, *5*, e286; b) J. Zhang, S. Duan, C. You, J. Wang, H. Liu, S. Guo, W. Zhang, R. Yang, *J. Mater. Chem. A* **2020**, *8*, 22240; c) J. Zhang, C. You, W. Zhang, J. Wang, S. Guo, R. Yang, Y. Xu, *Electrochim. Acta* **2017**, *250*, 159.

[7] J. Zhang, C. You, H. Lin, J. Wang, *Energy Environ. Mater.* **2021**, *5*, 731.

[8] a) J. Zhang, C. You, J. Wang, H. Xu, C. Zhu, S. Guo, W. Zhang, R. Yang, Y. Xu, *Chem. Eng. J.* **2019**, *368*, 340; b) D. Zhang, S. Wang, R. Hu, J. Gu, Y. Cui, B. Li, W. Chen, C. Liu, J. Shang, S. Yang, *Adv. Funct. Mater.* **2020**, *30*, 2002471.

[9] a) J. Wang, J. Zhang, S. Cheng, J. Yang, Y. Xi, X. Hou, Q. Xiao, H. Lin, *Nano Lett.* **2021**, *21*, 3245; b) J. Wang, J. Zhang, S. Duan, L. Jia, Q. Xiao, H. Liu, H. Hu, S. Cheng, Z. Zhang, L. Li, W. Duan, Y. Zhang, H. Lin, *Nano Lett.* **2022**, *22*, 8008; c) H. Ye, Z. J. Zheng, H. R. Yao, S. C. Liu, T. T. Zuo, X. W. Wu, Y. X. Yin, N. W. Li, J. J. Gu, F. F. Cao, Y. G. Guo, *Angew. Chem., Int. Ed. Engl.* **2019**, *58*, 1094.

[10] a) B. Qin, Y. Cai, P. Wang, Y. Zou, J. Cao, J. Qi, *Energy Storage Mater.* **2022**, *47*, 345; b) L. Wang, W. Hua, X. Wan, Z. Feng, Z. Hu, H. Li, J. Niu, L. Wang, A. Wang, J. Liu, X. Lang, G. Wang, W. Li, Q. H. Yang, W. Wang, *Adv. Mater.* **2022**, 2110279; c) L. Jia, J. Wang, Z. Chen, Y. Su, W. Zhao, D. Wang, Y. Wei, K. Jiang, J. Wang, Y. Wu, J. Li, W. Duan, S. Fan, Y. Zhang, *Nano Res.* **2019**, *12*, 1105; d) K. Xu, M. Zhu, X. Wu, J. Liang, Y. Liu, T. Zhang, Y. Zhu, Y. Qian, *Energy Storage Mater.* **2019**, *23*, 587; e) J. Wang, H. Hu, S. Duan, Q. Xiao, J. Zhang, H. Liu, Q. Kang, L. Jia, J. Yang, W. Xu, H. Fei, S. Cheng, L. Li, M. Liu, H. Lin, Y. Zhang, *Adv. Funct. Mater.* **2021**, 2110468.

[11] a) J. Wang, S. Cheng, W. Li, L. Jia, Q. Xiao, Y. Hou, Z. Zheng, H. Li, S. Zhang, L. Zhou, M. Liu, H. Lin, Y. Zhang, *Nano Energy* **2017**, *40*, 390; b) J. Wang, J. Yang, Q. Xiao, J. Zhang, T. Li, L. Jia, Z. Wang, S. Cheng, L. Li, M. Liu, H. Liu, H. Lin, Y. Zhang, *Adv. Funct. Mater.* **2020**, *31*, 2007434.

[12] a) J. Wang, L. Li, H. Hu, H. Hu, Q. Guan, M. Huang, L. Jia, H. Adenusi, K. V. Tian, J. Zhang, S. Passerini, H. Lin, *ACS Nano* **2022**, *16*, 17729; b) J. Wang, J. Zhang, J. Wu, M. Huang, L. Jia, L. Li, Y. Zhang, H. Hu, F. Liu, Q. Guan, M. Liu, H. Adenusi, H. Lin, S. Passerini, *Adv. Mater.* **2023**, *35*, 2302828.

[13] a) J. Wang, L. Jia, S. Duan, H. Liu, Q. Xiao, T. Li, H. Fan, K. Feng, J. Yang, Q. Wang, M. Liu, J. Zhong, W. Duan, H. Lin, Y. Zhang, *Energy Storage Mater.* **2020**, *28*, 375; b) J. Wang, L. Jia, H. Lin, Y. Zhang, *ChemSusChem* **2020**, *13*, 3404.

[14] a) Z. Li, *Nano Energy* **2023**, *113*, 108527; b) Z. Li, B. Li, Q. Li, *Adv. Mater.* **2023**, *35*, 2211103.

[15] X. Gao, Y.-N. Zhou, D. Han, J. Zhou, D. Zhou, W. Tang, J. B. Goodenough, *Joule* **2020**, *4*, 1864.

[16] L. Ren, K. Sun, Y. Wang, A. Kumar, J. Liu, X. Lu, Y. Zhao, Q. Zhu, W. Liu, H. Xu, X. Sun, *Adv. Mater.* **2023**, *36*, 2310547.

[17] a) B. Lu, Z. Min, X. Xiao, B. Wang, B. Chen, G. Lu, Y. Liu, R. Mao, Y. Song, X. X. Zeng, Y. Sun, J. Yang, G. Zhou, *Adv. Mater.* **2023**, *36*, 2309264; b) C. Pei, J. Gong, *Science* **2021**, *371*, 1203.

[18] H. Zhang, B. Song, W. Zhang, B. An, L. Fu, S. Lu, Y. Cheng, Q. Chen, K. Lu, *Angew. Chem., Int. Ed.* **2023**, *135*, 202217009.

[19] X. Zhang, X. Li, Y. Zhang, X. Li, Q. Guan, J. Wang, Z. Zhuang, Q. Zhuang, X. Cheng, H. Liu, J. Zhang, C. Shen, H. Lin, Y. Wang, L. Zhan, L. Ling, *Adv. Funct. Mater.* **2023**, *33*, 2302624.

[20] J. Xu, V. Koverga, A. Phan, A. min Li, N. Zhang, M. Baek, C. Jayawardana, B. L. Lucht, A. T. Ngo, C. Wang, *Adv. Mater.* **2023**, *36*, 2306462.

[21] Z. Li, L. P. Hou, N. Yao, X. Y. Li, Z. X. Chen, X. Chen, X. Q. Zhang, B. Q. Li, Q. Zhang, *Angew. Chem., Int. Ed.* **2023**, *62*, 202303363.

[22] Y. Chen, Y. Yao, W. Zhao, L. Wang, H. Li, J. Zhang, B. Wang, Y. Jia, R. Zhang, Y. Yu, J. Liu, *Nat. Commun.* **2023**, *14*, 7487.

[23] J. Wang, L. Jia, H. Liu, C. Wang, J. Zhong, Q. Xiao, J. Yang, S. Duan, K. Feng, N. Liu, W. Duan, H. Lin, Y. Zhang, *ACS Appl. Mater. Interfaces* **2020**, *12*, 12727.

[24] J. Zhang, L. Jia, H. Lin, J. Wang, *Adv. Energy Sustainability Res.* **2022**, *3*, 2100187.

[25] a) J. Wang, L. Jia, J. Zhong, Q. Xiao, C. Wang, K. Zang, H. Liu, H. Zheng, J. Luo, J. Yang, H. Fan, W. Duan, Y. Wu, H. Lin, Y. Zhang, *Energy Storage Mater.* **2019**, *18*, 246; b) J. Wang, J. Zhang, S. Duan, T. Li, L.

Jia, H. Liu, L. Li, S. Cheng, H. Hu, M. Huang, H. Hu, S. Zhang, Q. Xiao, H. Lin, *Chem. Eng. J.* **2022**, *429*, 132352.

[26] a) M. Menzinger, R. Wolfgang, *Angew. Chem., Int. Ed. Engl.* **2003**, *8*, 438; b) J. Zhang, R. He, Q. Zhuang, X. Ma, C. You, Q. Hao, L. Li, S. Cheng, L. Lei, B. Deng, X. Li, H. Lin, J. Wang, *Adv. Sci.* **2022**, *9*, 2202244.

[27] H. Zhang, J. Chen, Z. Li, Y. Peng, J. Xu, Y. Wang, *Adv. Funct. Mater.* **2023**, *33*, 2304433.

[28] Y. Yang, C. Zhang, Z. Mei, Y. Sun, Q. An, Q. Jing, G. Zhao, H. Guo, *Nano Res.* **2023**, *16*, 9289.

[29] T. Ma, Y. Ni, Q. Wang, W. Zhang, S. Jin, S. Zheng, X. Yang, Y. Hou, Z. Tao, J. Chen, *Angew. Chem., Int. Ed.* **2022**, *61*, 202207927.

[30] K. Yan, H. W. Lee, T. Gao, G. Zheng, H. Yao, H. Wang, Z. Lu, Y. Zhou, Z. Liang, Z. Liu, S. Chu, Y. Cui, *Nano Lett.* **2014**, *14*, 6016.

[31] X. Jiao, Y. Wang, O. O. Kapitanova, X. Xu, V. S. Volkov, Y. Liu, Z. Song, A. Matic, S. Xiong, *Energy Storage Mater.* **2023**, *61*, 102916.

[32] J. Tan, W. Yao, M. Ye, J. Shen, *J. Mater. Chem. A* **2022**, *10*, 18577.

[33] Z. Du, X. Chen, W. Hu, C. Chuang, S. Xie, A. Hu, W. Yan, X. Kong, X. Wu, H. Ji, L. J. Wan, *J. Am. Chem. Soc.* **2019**, *141*, 3977.

[34] C. Ma, Y. Zhang, Y. Feng, N. Wang, L. Zhou, C. Liang, L. Chen, Y. Lai, X. Ji, C. Yan, W. Wei, *Adv. Mater.* **2021**, *33*, 2100171.

[35] a) J. Zhang, C. You, J. Wang, S. Guo, W. Zhang, R. Yang, P. Fu, *Chem-ElectroChem* **2019**, *6*, 5051; b) P. Qiu, Y. Yao, W. Li, Y. Sun, Z. Jiang, B. Mei, L. Gu, Q. Zhang, T. Shang, X. Yu, J. Yang, Y. Fang, G. Zhu, Z. Zhang, X. Zhu, T. Zhao, W. Jiang, Y. Fan, L. Wang, B. Ma, L. Liu, Y. Yu, W. Luo, *Nano Lett.* **2021**, *21*, 700; c) S. F. Ng, M. Y. L. Lau, W. J. Ong, *Adv. Mater.* **2021**, *33*, 2008654.

[36] M. Zhang, W. Chen, L. Xue, Y. Jiao, T. Lei, J. Chu, J. Huang, C. Gong, C. Yan, Y. Yan, Y. Hu, X. Wang, J. Xiong, *Adv. Energy Mater.* **2019**, *10*, 1903008.

[37] C. Lu, Y. Chen, Y. Yang, X. Chen, *Nano Lett.* **2020**, *20*, 5522.

[38] a) J. Wang, S. Cheng, L. Li, L. Jia, J. Wu, X. Li, Q. Guan, H. Hu, J. Zhang, H. Lin, *Chem. Eng. J.* **2022**, *446*, 137291; b) J. Wang, J. Yang, Q. Xiao, L. Jia, H. Lin, Y. Zhang, *ACS Appl. Mater. Interfaces* **2019**, *11*, 30500; c) J. Zhang, R. He, L. Jia, C. You, Y. Zhang, M. Liu, N. Tian, H. Lin, J. Wang, *Adv. Funct. Mater.* **2023**, *33*, 2305674.

[39] L. Jia, J. Wang, S. Ren, G. Ren, X. Jin, L. Kao, X. Feng, F. Yang, Q. Wang, L. Pan, Q. Li, Y. s. Liu, Y. Wu, G. Liu, J. Feng, S. Fan, Y. Ye, J. Guo, Y. Zhang, *Energy Environ. Mater.* **2020**, *4*, 222.

[40] X. Meng, X. Liu, X. Fan, X. Chen, S. Chen, Y. Meng, M. Wang, J. Zhou, S. Hong, L. Zheng, G. Shi, C. W. Bielawski, J. Geng, *Adv. Sci.* **2022**, *9*, 2103773.

[41] Y. Li, G. Chen, J. Mou, Y. Liu, S. Xue, T. Tan, W. Zhong, Q. Deng, T. Li, J. Hu, C. Yang, K. Huang, M. Liu, *Energy Storage Mater.* **2020**, *28*, 196.

[42] S. Zhang, X. Ao, J. Huang, B. Wei, Y. Zhai, D. Zhai, W. Deng, C. Su, D. Wang, Y. Li, *Nano Lett.* **2021**, *21*, 9691.

[43] S. Xie, X. Chen, C. Wang, Y. R. Lu, T. S. Chan, C. H. Chuang, J. Zhang, W. Yan, S. Jin, H. Jin, X. Wu, H. Ji, *Small* **2022**, *18*, 2200395.

[44] a) R. Xiao, T. Yu, S. Yang, K. Chen, Z. Li, Z. Liu, T. Hu, G. Hu, J. Li, H.-M. Cheng, Z. Sun, F. Li, *Energy Storage Mater.* **2022**, *51*, 890; b) J. Sun, Y. Liu, L. Liu, S. He, Z. Du, K. Wang, L. Xie, H. Du, W. Ai, *Nano Lett.* **2022**, *22*, 3728.

[45] Z. Yi, F. Su, L. Dai, Z. Wang, L. Xie, Z. Zuo, X. Chen, Y. Liu, C.-m. Chen, *Energy Storage Mater.* **2022**, *47*, 327.

[46] Y. Ding, Q. Cheng, J. Wu, T. Yan, Z. Shi, M. Wang, D. Yang, P. Wang, L. Zhang, J. Sun, *Adv. Mater.* **2022**, *34*, 2202256.

[47] X. Han, Z. Zhang, X. Xu, *J. Mater. Chem. A* **2021**, *9*, 12225.

[48] Z. Han, S. Zhao, J. Xiao, X. Zhong, J. Sheng, W. Lv, Q. Zhang, G. Zhou, H. M. Cheng, *Adv. Mater.* **2021**, *33*, 2105947.

[49] G. Zhou, S. Zhao, T. Wang, S. Z. Yang, B. Johannessen, H. Chen, C. Liu, Y. Ye, Y. Wu, Y. Peng, C. Liu, S. P. Jiang, Q. Zhang, Y. Cui, *Nano Lett.* **2020**, *20*, 1252.

[50] Y. Feng, B. Zhong, R. Zhang, M. Peng, Z. Hu, Z. Wu, N. Deng, W. Zhang, K. Zhang, *Adv. Energy Mater.* **2023**, *13*, 2203912.

[51] L. Luo, K. Chen, H. Chen, H. Li, R. Cao, X. Feng, W. Chen, Y. Fang, Y. Cao, *Adv. Mater.* **2023**, *36*, 2308881.

[52] N. Sun, R. Li, Y. Zhao, H. Zhang, J. Chen, J. Xu, Z. Li, X. Fan, X. Yao, Z. Peng, *Adv. Energy Mater.* **2022**, *12*, 2200621.

[53] a) J. Wang, H. Hu, S. Duan, Q. Xiao, J. Zhang, H. Liu, Q. Kang, L. Jia, J. Yang, W. Xu, H. Fei, S. Cheng, L. Li, M. Liu, H. Lin, Y. Zhang, *Adv. Funct. Mater.* **2021**, *32*, 2110468; b) J. Wang, H. Hu, J. Zhang, L. Li, L. Jia, Q. Guan, H. Hu, H. Liu, Y. Jia, Q. Zhuang, S. Cheng, M. Huang, H. Lin, *Energy Storage Mater.* **2022**, *52*, 210.

[54] L. Zhang, X. Zhao, Z. Yuan, M. Wu, H. Zhou, *J. Mater. Chem. A* **2021**, *9*, 3855.

[55] D. He, W. Cui, X. Liao, X. Xie, M. Mao, X. Sang, P. Zhai, Y. Zhao, Y. Huang, W. Zhao, *Adv. Sci.* **2022**, *9*, 2105656.

[56] J. Wang, L. Li, H. Hu, H. Hu, Q. Guan, M. Huang, L. Jia, H. Adenusi, K. V. Tian, J. Zhang, S. Passerini, H. Lin, *ACS Nano* **2022**, *16*, 17729.

[57] P. Zhai, T. Wang, W. Yang, S. Cui, P. Zhang, A. Nie, Q. Zhang, Y. Gong, *Adv. Energy Mater.* **2019**, *9*, 1804019.

[58] Y. Sun, J. Zhou, H. Ji, J. Liu, T. Qian, C. Yan, *ACS Appl. Mater. Interfaces* **2019**, *11*, 32008.

[59] Z. L. Yang, Y. Dang, P. B. Zhai, Y. Wei, Q. Chen, J. H. Zuo, X. K. Gu, Y. Yao, X. G. Wang, F. F. Zhao, J. L. Wang, S. B. Yang, P. Z. Tang, Y. J. Gong, *Adv. Energy Mater.* **2022**, *12*, 2103368.

[60] C. L. Song, Z. H. Li, L. Y. Ma, M. Z. Li, S. Huang, X. J. Hong, Y. P. Cai, Y. Q. Lan, *ACS Nano* **2021**, *15*, 13436.

[61] J. Wang, H. Liu, J. Zhang, Q. Xiao, C. Wang, Y. Zhang, M. Liu, Q. Kang, L. Jia, D. Wang, Q. Li, W. Duan, H. Adenusi, S. Passerini, Y. Zhang, H. Lin, *Energy Storage Mater.* **2024**, *67*, 103289.

[62] C. L. Song, Z. H. Li, L. Y. Ma, M. Z. Li, S. Huang, X. J. Hong, Y. P. Cai, Y. Q. Lan, *ACS Nano* **2021**, *15*, 13436.

[63] Y. Meng, D. Zhou, R. Liu, Y. Tian, Y. Gao, Y. Wang, B. Sun, F. Kang, M. Armand, B. Li, G. Wang, D. Aurbach, *Nat. Energy* **2023**, *8*, 1023.